Image Grating Metrology Using a Fresnel Zone Plate

by

Chulmin Joo

B.S. Aerospace Engineering, Korea Advanced Institute of Science and Technology (1998)

Submitted to the Department of Mechanical Engineering
in partial fulfillment of the requirements for the degree of

Master of Science in Mechanical Engineering

at the

MASSACHUSETTS INSTITUTE OF TECHNOLOGY

September 2003

Author .....
Department of Mechanical Engineering
August 18, 2003

Certified by .....
Mark L. Schattenburg
Principal Research Scientist
Thesis Supervisor

Accepted by .....
Ain A. Sonin
Chairman, Department Committee on Graduate Students

Image Grating Metrology
Using a Fresnel Zone Plate

by

Chulmin Joo

Submitted to the Department of Mechanical Engineering
on August 18, 2003, in partial fulfillment of the
requirements for the degree of
Master of Science in Mechanical Engineering

Abstract

Scanning-beam interference lithography (SBIL) is a novel concept for nanometer-accurate grating fabrication. It can produce gratings with nanometer phase accuracy over large area by scanning a photoresist-coated substrate under phase-locked image grating. For the successful implementation of the SBIL, it is crucial to measure the spatial period, phase, and distortion of the image grating accurately, since it enables the precise stitching of subsequent scans.

This thesis describes the efforts to develop an image grating metrology that is capable of measuring a wide range of image periods, regardless of changes in grating orientation. In order to satisfy the conditions, the use of a Fresnel zone plate is proposed. The Fresnel zone plate is a circularly symmetric diffraction grating that contains a wide range of spatial frequencies. The work begins with a basic understanding of the zone plate, followed by the physics of the image metrology. Closed mathematical solution is obtained to describe the diffraction pattern of incident plane waves by a Fresnel zone plate. For a given zone plate, a range of image periods that can be measured is also investigated. The question regarding to contrast variation of optical power by varying image period is also discussed.

The detailed theoretical analysis is followed by the experiments designed and performed to verify the findings. Period measurements are conducted in two cases: homodyne and heterodyne measurements. In the homodyne case, two different image periods are measured using the same amplitude zone plate. In the heterodyne measurement, the zone plate is installed in the current SBIL prototype system, the Nanoruler, and is used to measure the period of the image grating with fringes that moves at frequency difference between two beams. The contrast variation is also verified by the experiment.

With the two conditions for image metrology to satisfy: immune to grating orientations and capability of measuring a wide range of periods, the use of a zone plate would be an excellent choice. However, one should be careful to use a properly designed zone plate such that the image period to be measured is within the range of high contrast for a given zone plate.

Thesis Supervisor: Mark L. Schattenburg
Title: Principal Research Scientist

Acknowledgments

Firstly, I wish to thank my advisor, Dr. Schattenburg, for giving me a chance to work at the *MIT Space Nanotechnology Laboratory*. His strong physics and engineering intuitions always surprise me, and his incessant encouragement and optimistic attitude motivate me. Dr. Heilmann has been always kind to discuss my ideas and questions, and review my mathematical formulations. A lot of times, he enlightened me with his profound knowledge on physics. Dr. Pati was generous in sharing his optics knowledge and skills with me.

I have bugged Carl Chen and Paul Konkola quite often with a lot of stupid questions. Carl has always kindly answered my questions, and even greeted me with a good sense of humor. I promise him to buy a big Korean meal, and bring him to a Korean dance club in Seoul. Paul's knowledge and experience on systems and controls are invincible. I feel sorry that I lost the chance to learn more from them. Congratulations on your graduations.

I have been lucky to have three great office mates for the past two years. Craig is one of the most diligent and cheerful friends that I have. We have spent a lot of time talking about our research and future career goals. Yanxia's care and warmth to me is really grateful since I joined our group. Without Juan's expertise on electronics, I couldn't have finished the work. He has worked extremely hard on the Nanoruler, and now he is essential for the implementation of the next-generation Nanoruler.

I am also grateful to Bob Fleming and Ed Murphy for their generous assistance on many occasions, and Alexander Liddle and Erik H. Anderson at Lawrence Berkeley National Laboratory for providing the zone plates for our research.

I appreciate Euiheon Chung of his encouragement and care at KAIST and MIT. Ever since I met him, he has been a mentor, a role-model, and a good brother to me. I sincerely hope that he has great days with his wife and new baby, Haewon. Soon-Jo Chung is one of my best friends. He has shown me unconditional care, since he picked me up at the airport. I wouldn't forget the Miso soap that he made for me at my first day in the U.S. My current roommates, Juhyun Park and Eun Suk Suh, are also

thankful to take care of me for one year. Ilyong Kim is expected to be a father soon. Yoonsun Chung is taking a closer step to become an MIT PhD. I wish her the best luck.

On a more personal note, I would like to thank Mihwa for her unflagging love and support for me. She has provided me the courage and motivation to get through the obstacles and difficulties here at MIT, especially a few months ago. I thank God for giving me the chance to meet her in my life. Lastly, but mostly, I am forever indebted to my parents and future parents-in-law. Without their generous love, guidance, and support, I could not have survived here.

The work documented in this thesis was supported by DARPA under Grant No. DAAG55-98-1-0130 and NASA under Grant No. NAG5-5271.

Contents

List of Figures

List of Tables

Chapter 1

Introduction

Gratings with nanometer phase accuracy enable important advances in metrology, electro-optics, spectroscopy, diffractive optics, and many other fields. Paul Konkola and Carl Chen described several examples of the application of gratings [19], [22]. In particular, our perspective is to use the fiducial gratings as the metrological standards in semiconductor pattern placement metrology and grating-based displacement measuring interferometry.

Interference lithography (IL) is one of the methods for fabricating gratings [2]. The IL method exposes the standing wave pattern formed by the interference of two coherent laser beams onto a photoresist-coated substrate. The linear grating pattern produced in space by the interference of two beams is defined as image grating, and its nominal period is given by,

$$\Lambda = \frac{\lambda}{2\sin\theta} \tag{1.1}$$

where λ is the wavelength of light, and 2θ is the angle between the beams (Fig. 1-1). In Figure 1-2, two types of "traditional" interference lithography systems are depicted. The configuration (a) uses the interference of two spherical waves generated by the small pinhole. Since the spherical waves generated by a point-source-like pinhole are spatially-coherent, the pattern can be regarded as very coherent. However, it inherently has hyperbolic distortions that limits the size of linear grating. Juan

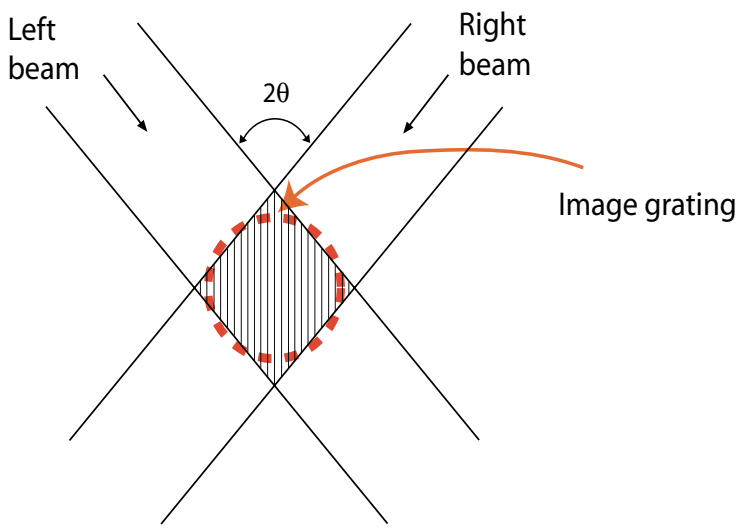

Figure 1-1: The standing wave patten produced by interference of two beams is defined as an image grating.

Ferrera has analyzed the distortions in the interference lithography [3], and Chen has demonstrated that the region of subnanometer nonlinear phase is less than 2.8 mm in diameter for the MIT IL set up for 400 nm gratings [19]. The configuration (b) exploits the interference of two plane waves generated by collimating lenses, but it also has a problem in that optics defects (typically $\sim \lambda/10$ over the full optics size) distort the wavefronts of the beams, which consequently reduce the grating quality.

1.1 Scanning-Beam Interference Lithography

In order to resolve the limitations of the "traditional" IL setup, Mark Schattenburg has proposed the concept of Scanning-Beam Interference Lithography (SBIL) [1], and its prototype tool named the Nanoruler is under development in our lab. Figure 1-3 depicts the concept of SBIL. The optics closely resemble those of "traditional" IL, but the image grating is much smaller than the total desired pattern size. By using small laser beams, SBIL can minimize wavefront distortions caused by the optics, and fabricate phase accurate gratings over large areas by scanning a photoresist-coated substrate under the phase-locked image grating pattern. Figure 1-4 shows the SBIL scan method. After one scan, the stage steps over by an integer number of grating

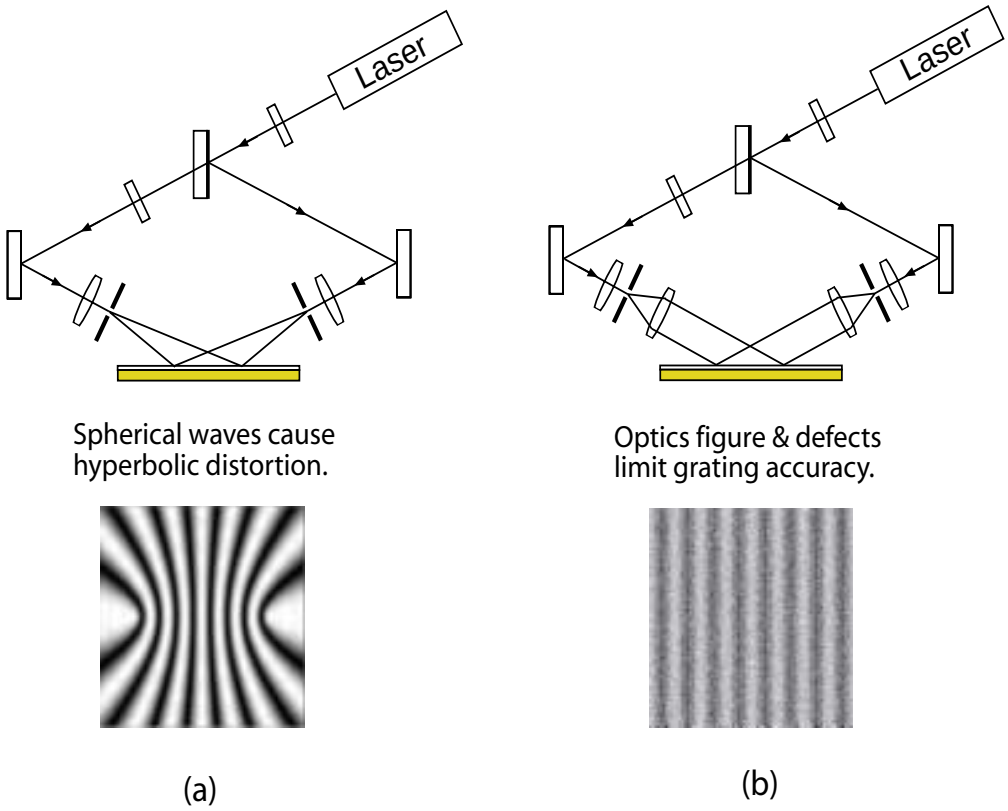

Figure 1-2: Traditional interference lithography. Configuration (a) can fabricate large gratings by using the interference pattern of two spherical waves. However, the interference pattern has hyperbolic distortions. Configuration (b) uses the interference of two plane waves, but it also suffers from wavefront distortion caused by the optics.

periods and reverses direction for subsequent scans. Several important technological breakthroughs have been made and reported during the development of the tool, and they include beam alignment, image metrology, beam steering system, digital heterodyne fringe locking, active vibration isolation, and so on. [4], [5], [6], [7].

1.2 Image Grating Metrology

To fabricate large area gratings, it is required that the stage steps over by an integer number of image periods, and scans in the reverse direction. Thus, measuring image grating period is crucial since it ensures the precise stitching of subsequent scans. Furthermore, *in-situ* characterization of the spatial period, phase, and orientation of the image grating is essential to improve SBIL performance.

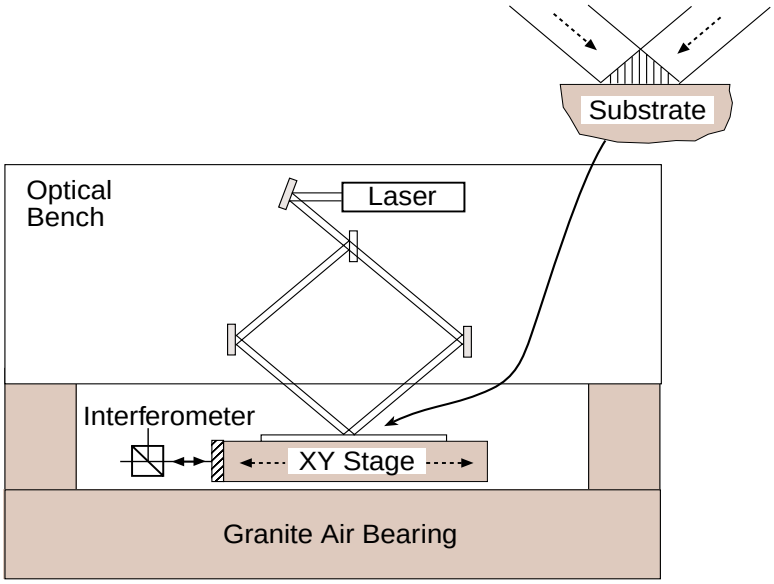

Figure 1-3: Scanning-beam interference lithography. SBIL can fabricate nanometer phase accurate gratings over large areas by scanning a photoresist-coated substrate under the phase-locked image grating.

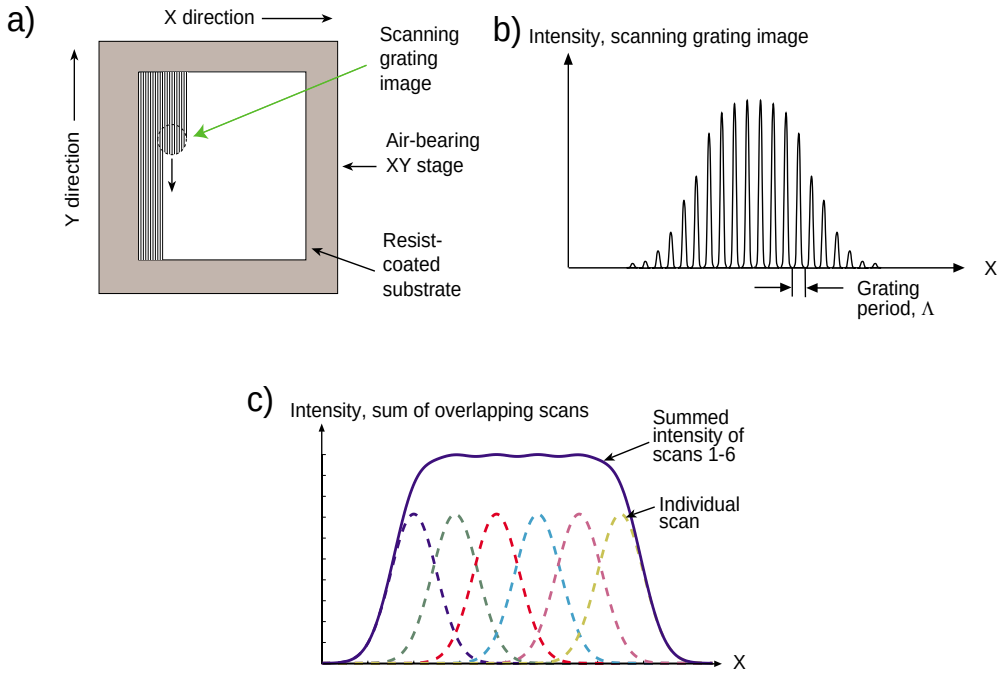

Figure 1-4: SBIL scan method. (a) To ensure accurate stitching of adjacent scans, the stage steps over by an integer number of grating periods. (b) Gaussian intensity envelope. (c) Beam overlapping to create a uniform exposure dose.

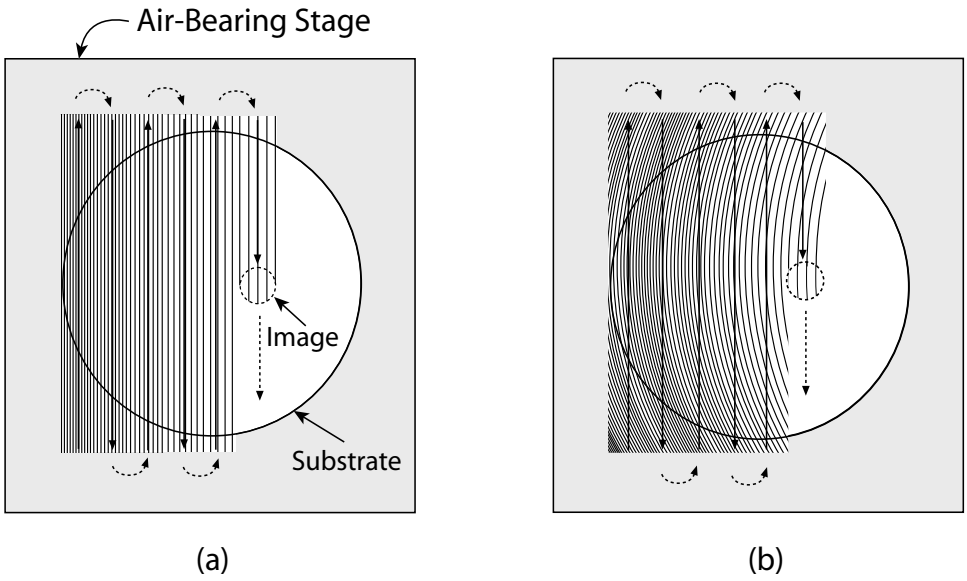

Figure 1-5: General gratings fabricated by SBIL. It can be achieved by using the capability of SBIL step-and-scan and varying orientation and incident angles of the beams. (a) Linear chirped grating. (b) Curved chirped grating.

The next-generation Nanoruler should be also able to pattern linear or curved chirped gratings (Figure. 1-5) [10]. These general patterns can be fabricated by varying incident angles and orientation of the laser beams during the operation. The application of the chirped gratings in our case is to use them as the reflection gratings to diffract x-rays in the Constellation-X Spectroscopy X-ray Telescope [8], [9].

Previously, researchers have attempted to use detectors apertured with extremely narrow slits to characterize image grating irradiance distributions [11]. However, the amount of light leaking through narrow slits decreases dramatically as the sub-micron domain approaches, and aligning the slit along the image grating lines is extremely difficult.

Chen *et al.* [4] has also proposed using interferometry with a beamsplitter. Currently, a specially designed beamsplitter is set up to the Nanoruler. Figure 1-6 demonstrates the principle of operation of the beamsplitter scheme. The beamsplitter is mounted on the X-Y stage such that the interference of the reflected and transmitted beams can be measured at a photo-detector. Scanning across the interference fringe lines leads to relative optical path difference between two beams, which results in sinusoidal intensity variation at the photo-detector. Therefore, image grating period

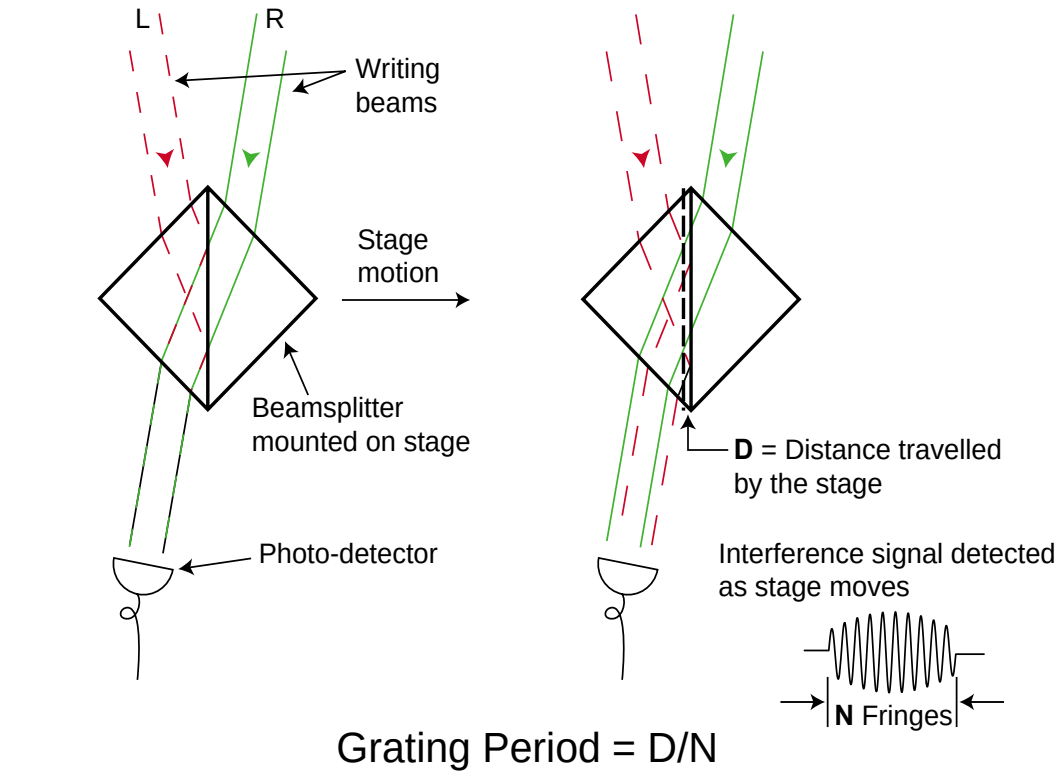

Figure 1-6: Image grating period measurement using a beamsplitter. The beams interfere at the photo-detector, and the interference signal changes by scanning the beamsplitter.

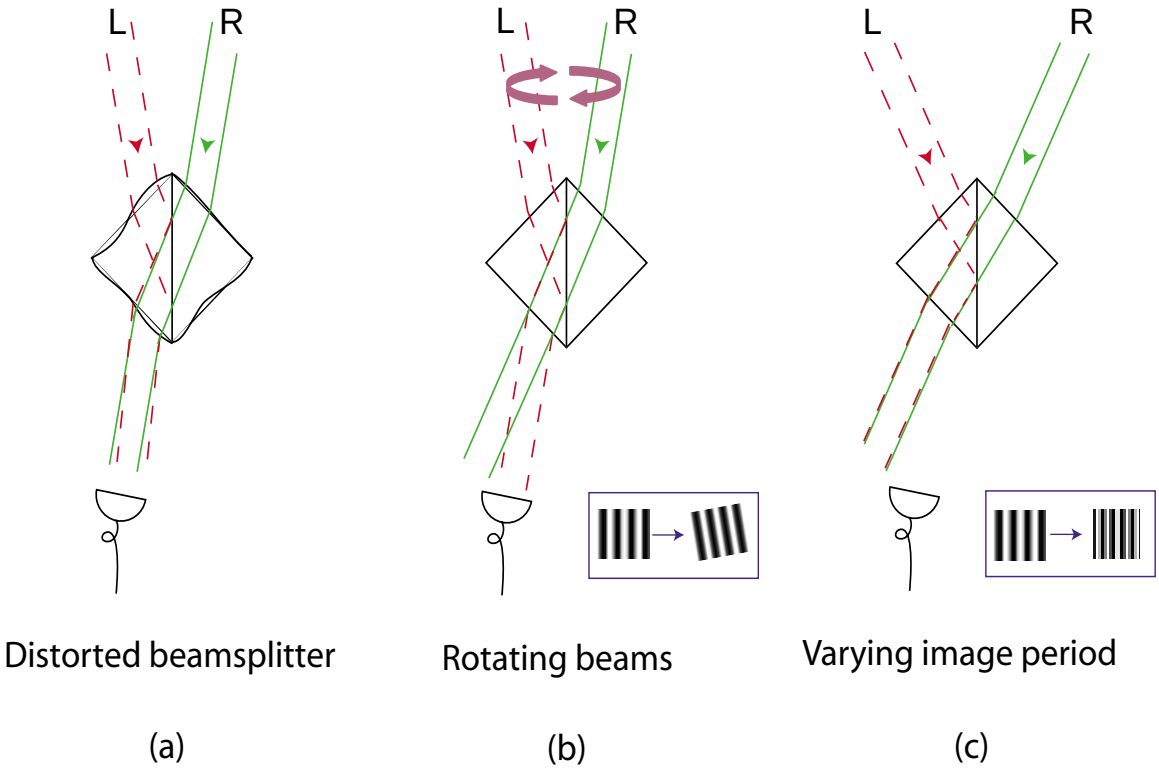

Figure 1-7: Limitations of the beamsplitter scheme.

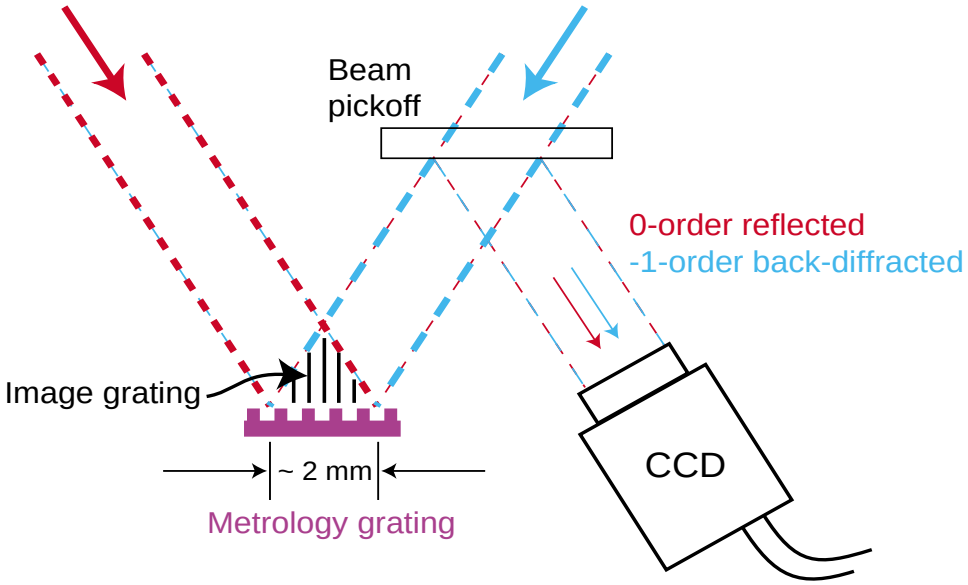

Figure 1-8: SBIL wavefront metrology. A metrology grating with an ideal linear spatial phase is used under the Littrow condition. The reflected and back-diffracted beams interfere at a CCD camera.

can be obtained directly by dividing the displacement traveled by the beamsplitter by the number of oscillations measured at the photo-detector. However, it has several limitations, though it proves very effective at measuring the spatial period and phase of the image grating.

Any distortion in the beamsplitter leads to distortions of the wavefronts of each beam, which consequently result in an inaccurate measurement of image grating characteristics. Also, if the two beams rotate in order to vary grating line orientation, the beamsplitter scheme cannot be used because the transmitted and the reflected beams are no longer overlapped. The range in which the beamsplitter can be used is inherently limited. If incident angles vary during the operation, and become too large or too small, the overlapped beams will no longer be incident on the photo-detector unless the photo-detector is moved.

In order to accurately measure the nonlinear phase distortions in the image grating, the current Nanoruler exploits moiré-based interferometry using a metrology grating. The metrology grating is placed on the vacuum chuck, and it is used under the Littrow condition, where the zeroth-order beam from the left arm coincides with the -1st order back-diffracted beam from the right arm (Fig. 1-8). The beams in-

terfere and produce an interferogram that gets recorded by a charge-coupled-device (CCD) camera. Chen designed and implemented the wavefront metrology, and its detailed description can be found in Ref. [19].

1.3 Use of Fresnel Zone Plate for Image Grating Metrology

I propose to analyze a novel image grating metrology that exploits unique properties of a Fresnel zone plate. A Fresnel zone plate is a circularly symmetric diffractive structure that contains a wide range of spatial frequencies. Its axial symmetry enables us to characterize image gratings regardless of changes in grating line orientation. A broad range of image grating periods can also be measured due to the chirped feature of a Fresnel zone plate. Furthermore, a Fresnel zone plate can be manufactured with small form-factor. Its typical size is on the order of $\sim$200 μm in diameter. Namely, image grating characterization on a small size basis is possible. Indeed, the beamsplitter scheme discussed in the previous section essentially characterizes image gratings based on the averaged optical power over the entire image grating patch. However, the Fresnel zone plate scheme uses the optical power transmitted through the zone plate, so it can characterize an image grating based on a size on the same order of the zone plate.

This thesis consists of two parts: theory and experiment. In Chapter 2, I present the theoretical studies of image grating metrology using a Fresnel zone plate. Beginning with the basic understanding of the principle of the zone plate, diffraction of plane waves by a zone plate, the range of image periods that can be measured by a zone plate are discussed. Furthermore, in order to understand the effects of varying image period on the performance of the zone plate scheme, the optical power contrast variation is also studied. Throughout the analysis, scalar diffraction theory is used, and the incident waves are assumed to be coherent unit-amplitude plane waves.

Based on the analysis, three experiments are designed and conducted. In a ho-

modyne period measurement, a modified Mach-Zehnder interferometry has been designed, and image grating periods have been measured for two different incident angles. A heterodyne experiment has also been designed and performed. The image grating metrology is setup on the Nanoruler to measure image grating period, with fringes moving at frequency difference of two beams. The measured period is compared with that obtained by the beamsplitter scheme. Lastly, contrast variation is measured using the same set up as the homodyne period measurement.

Chapter 2

Theory

2.1 Fresnel zone plate

The Fresnel zone plate is a circularly symmetric diffraction grating composed of alternating opaque and transparent zones. Under plane wave illumination, the Fresnel zone plate diffracts the incident wave and focuses diffracted waves to different locations, or different focal points. The first-order diffraction waves, which have the highest intensity except for the zeroth-order plane wave, are focused to a point referred as the primary or the first-order focal point. Consider a circular grating illustrated in Fig. 2-1. If one draws a right triangle that has the primary focal length f as one side and the radius of any zone r_n as a second side, one can easily prove that

$$f^2 + r_n^2 = \left(f + \frac{n\lambda}{2} \right)^2 , \tag{2.1}$$

for constructive interference in the first-order to occur at the point f [12]. Upon expansion and consolidation of like terms, Equation (2.1) becomes

$$r_n^2 = n\lambda f + \frac{n^2\lambda^2}{4}. \tag{2.2}$$

The term $n^2\lambda^2/4$ represents spherical aberration, which can be ignored for $f \gg n\lambda/2$. Then, Equation (2.2) simplifies to

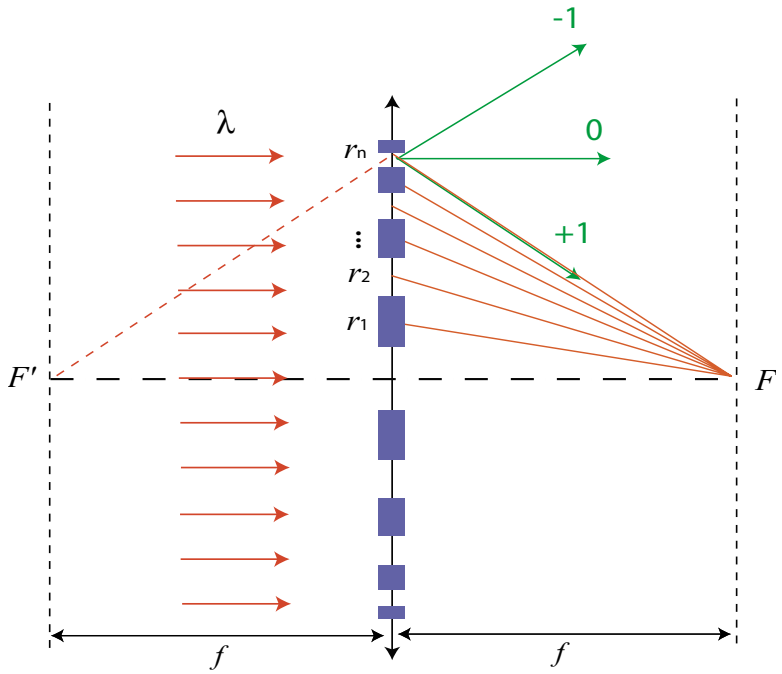

Figure 2-1: The Fresnel zone plate is a circularly symmetric diffraction grating composed of alternating opaque and transparent zones. It is designed such that its diffracted waves are focused to multiple focal points. In the Figure, the -1st order diffraction waves are focused to the primary or the first-order focal point F.

$$r_n \simeq \sqrt{n\lambda f}, \tag{2.3}$$

or

$$r_n^2 \simeq n\lambda f \tag{2.4}$$

showing that the first-order focus is achieved as successive zones increase in radius by $\sqrt{n}$, providing the desired prescription by which the radial grating period must decrease in order to provide common focus. The earliest known record regarding the demonstration of focusing light with alternatively opaque Fresnel zones is that of Lord Rayleigh in 1871 [13].

Equation (2.4) reveals that a Fresnel zone plate can be thought as a typical linear grating if it is expressed as a function of r^2. Figure 2-2 depicts the transmittance of a Fresnel zone plate denoted by $t(r^2)$. The $t(r^2)$ is a square wave with a period $2\lambda f$. It can thus be expressed as a Fourier series by

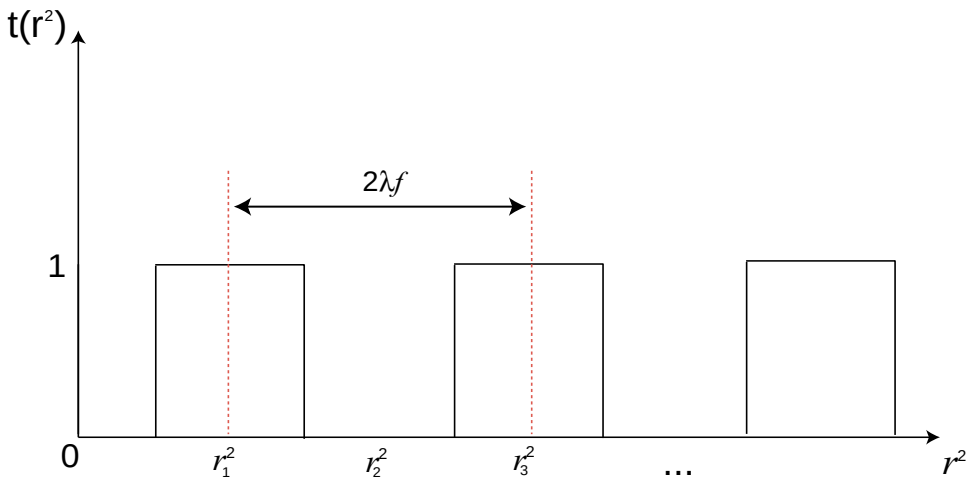

Figure 2-2: $r_n^2 = n\lambda f$. A Fresnel zone plate can be regarded as a square wave profile with a period of $2\lambda f$, if it is expressed as a function of r^2. Therefore, it can be expressed as a Fourier series.

$$t(r^2) = \sum_{n=-\infty}^{\infty} A_n \exp\left(jn\pi \frac{r^2}{\lambda f}\right). \tag{2.5}$$

Here,

$$A_n = \frac{\sin(n\pi/2)}{n\pi}, \tag{2.6}$$

and $A_0 = 1/2$ by L'Hopital's rule [14].

If one expands Eqn. (2.5), it becomes

$$\begin{aligned} t(r^2) = \cdots + \overbrace{A_{-3}\exp\left(-j\pi\frac{r^2}{\lambda(f/3)}\right)}^{\text{converging spherical wave}} + \overbrace{A_{-1}\exp\left(-j\pi\frac{r^2}{\lambda f}\right)}^{\text{converging spherical wave}} \\ + \underbrace{\frac{1}{2}}_{\text{plane wave}} + \underbrace{A_1\exp\left(j\pi\frac{r^2}{\lambda f}\right)}_{\text{diverging spherical wave}} + \underbrace{A_3\exp\left(j\pi\frac{r^2}{\lambda(f/3)}\right)}_{\text{diverging spherical wave}} + \cdots. \end{aligned} \tag{2.7}$$

As indicated, the transmittance of a Fresnel zone plate can be regarded as a planar section of the superposition of one plane wave and multiple converging and diverging spherical waves with different focal points (Fig. 2-3). Each term in Eqn. (2.7) has different intensity given by

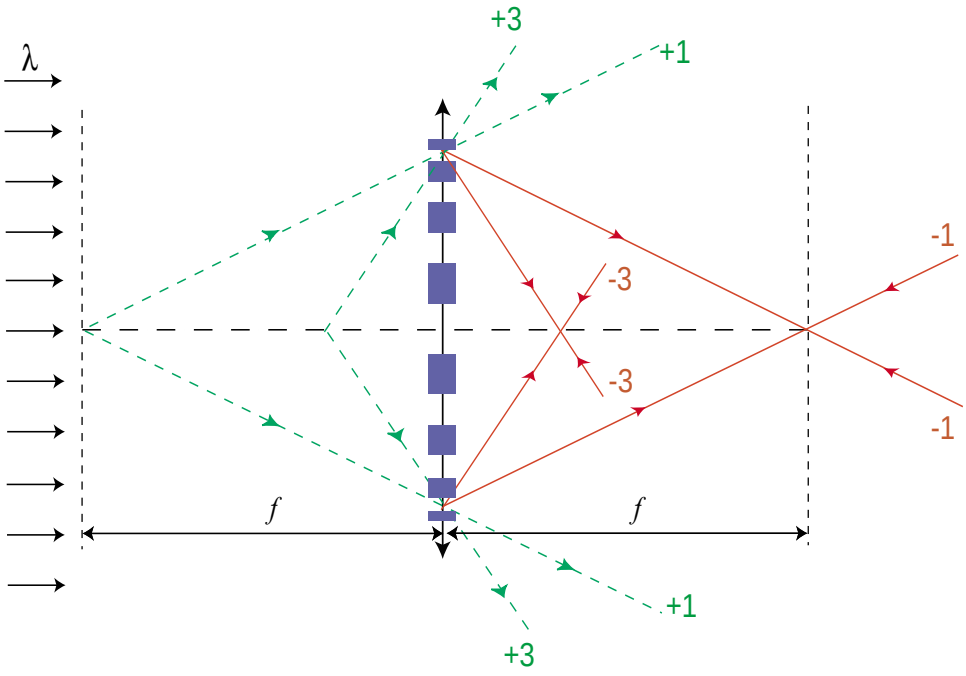

Figure 2-3: The Fresnel zone plate is represented as a superposition of multiple converging and diverging spherical waves with different focal points. In the Figure, only the ±1st and the ±3rd order spherical waves are shown for clarity.

$$I_n = |A_n|^2 I_0, \tag{2.8}$$

where I_0 represents the incident intensity. The ratio of the intensity of the nth order diffraction wave to the incident intenstiy is defined as the diffraction efficiency, and it is given by

$$\eta_n = \begin{cases} 0.25 & n = 0 \\ 1/n^2\pi^2 & n \text{ odd} \\ 0 & n \text{ even} \end{cases} \tag{2.9}$$

for a transmission Fresnel zone plate with 50% duty cycle. In other words, 25% of the incident intensity is in the 0th order, approximately 10% is diffracted into each of the ±1st orders, and so forth, whereas the Fresnel zone plate itself absorbs 50% of the incident intensity.

2.2 Diffraction of two plane waves by a Fresnel zone plate

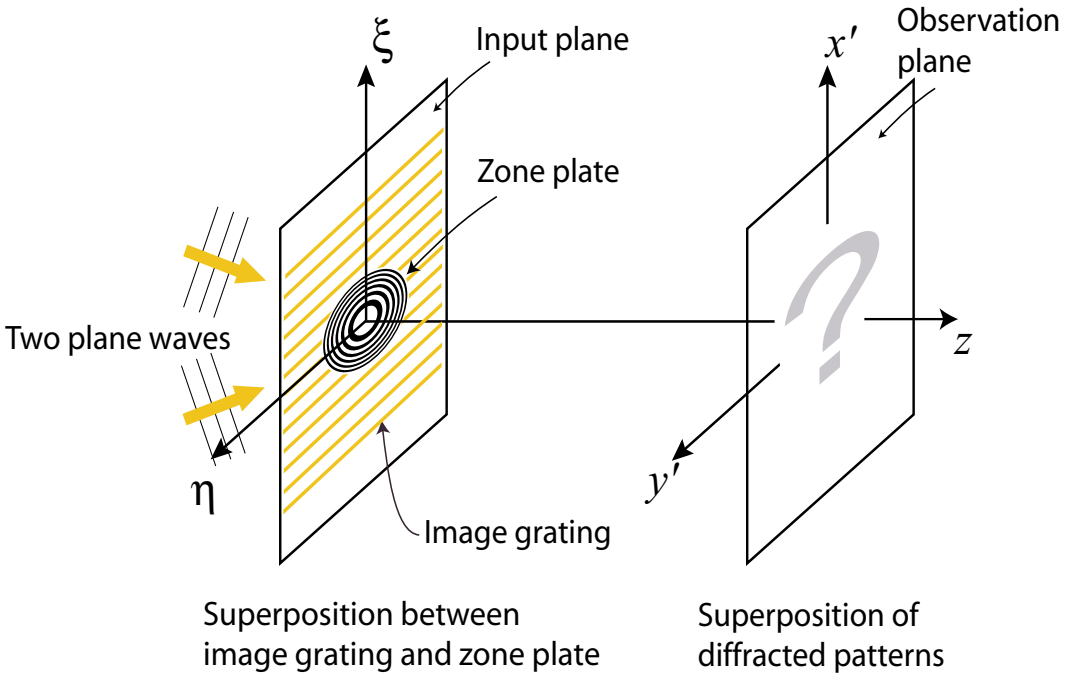

Figure 2-4: Diffraction geometry of a Fresnel zone plate and two plane waves. Two plane waves are incident on the input plane defined by (ξ, η), and diffracted by the Fresnel zone plate.

In order to understand the physics of image grating metrology using a Fresnel zone plate, it is necessary to study the diffraction of an image grating by a Fresnel zone plate and to find the relationship between image grating characteristics and the optical power of the diffraction pattern in the observation plane. Previously, I reported diffraction of an image grating by a Fresnel zone plate using the Fraunhofer diffraction approximation, which is valid for the far-field diffraction [17]. Here, I present the mathematical analysis in more general form by using the Fresnel diffraction approximation that can also be applicable for the near-field diffraction [15]. Moreover, the closed solution for the diffraction pattern in the observation plane is obtained.

Consider two coherent unit-amplitude plane waves incident on a Fresnel zone plate (Fig. 2-4). The amplitude transmittance functions of two plane waves are given by

$$f_1(\xi,\eta) = \exp\left(-j\frac{2\pi}{\lambda}\sin\theta_1\xi\right), \tag{2.10}$$

$$f_2(\xi,\eta) = \exp\left(j\frac{2\pi}{\lambda}\sin\theta_2\xi\right), \tag{2.11}$$

where λ is the wavelength of light, θ_1 and θ_2 are the incident angles of two plane waves relative to the z-axis. The time dependent factor, $\exp(-j\omega t)$, has been dropped for convenience.

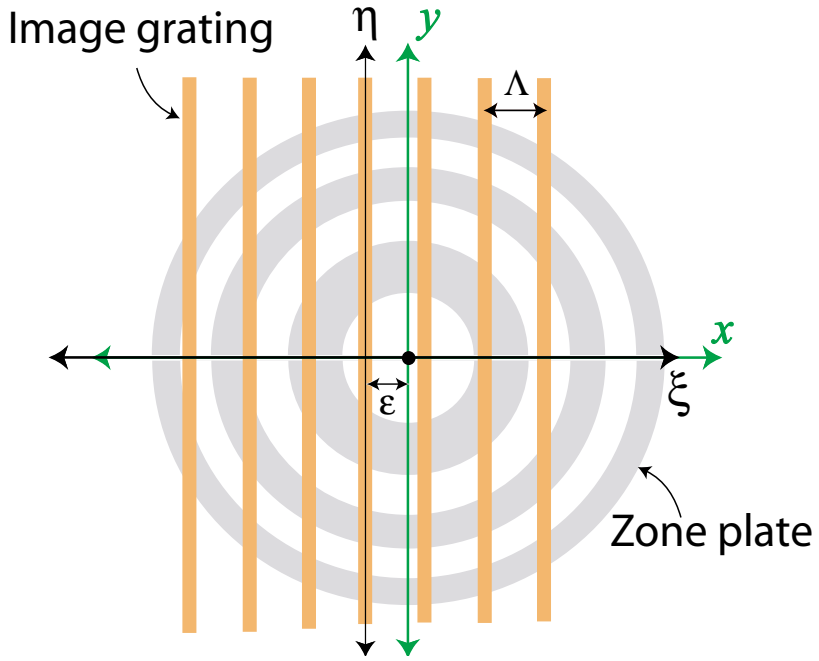

Figure 2-5: The image grating and the Fresnel zone plate in the input planes, (ξ,η) and (x,y). The image grating is phase-locked to the (ξ,η) plane, and the Fresnel zone plate is centered in the (x,y) plane. The (x,y) plane is displaced by ε relative to the (ξ,η) plane along the x axis.

In the (ξ,η) plane, an image grating is produced by the interference of two plane waves, and its irradiance is evaluated as

$$I_g(\xi,\eta) = 2 + 2\cos\left(\frac{2\pi}{\Lambda}\xi\right) \tag{2.12}$$

where

$$\Lambda = \frac{\lambda}{\sin\theta_1 + \sin\theta_2}.$$

Hence, the image grating has a period Λ in the (ξ, η) plane.

I also define the (x, y) plane at which the Fresnel zone plate is centered, and the two plane waves can then be expressed in the (x, y) plane as

$$f_1(x, y) = \exp\left(-j\frac{2\pi}{\lambda}\sin\theta_1(x + \varepsilon)\right), \tag{2.13}$$

$$f_2(x, y) = \exp\left(j\frac{2\pi}{\lambda}\sin\theta_2(x + \varepsilon)\right), \tag{2.14}$$

where ε refers to the displacement of the y axis of the plane (x, y) relative to the η axis of the plane (ξ, η) (Fig. 2-5).

As discussed earlier, the amplitude transmittance of a Fresnel zone plate is expressed as

$$t(x, y) = \sum_{n=-\infty}^{\infty} A_n \exp\left(jn\pi\frac{x^2 + y^2}{\rho^2}\right), \tag{2.15}$$

where ρ is a constant and equal to the radius of the first (or innermost) zone for a conventional Fresnel zone plate.

Two plane waves incident upon the Fresnel zone plate are diffracted and superimposed on the (x', y') plane that is parallel to the (x, y) plane and at normal distance z from it.

The free propagation of the amplitude transmittance on the (x, y) plane through the distance z can be studied in several ways [15]. Here, I use the classical approach based on the Huygens-Fresnel principle. Using the paraxial approximation, the classical form of the Fresnel diffraction equation is given by

$$E(x', y') = \frac{\exp(jkz)\exp\left(\frac{jk}{2z}(x'^2 + y'^2)\right)}{j\lambda z} \times$$
$$\int\int_{-\infty}^{\infty} t(x, y)\{f_1(x, y) + f_2(x, y)\}\exp\left(\frac{jk}{2z}(x^2 + y^2)\right)\exp\left(-j\frac{2\pi}{\lambda z}(xx' + yy')\right)dxdy \tag{2.16}$$

Here, k is the wave number defined by $2\pi/\lambda$. Equation (2.16) can be expressed as

$$E(x',y') = \frac{\exp(jkz)\exp\left(\frac{jk}{2z}(x'^2+y'^2)\right)}{j\lambda z} \times \int\int_{-\infty}^{\infty} u(x,y)\{f_1(x,y)+f_2(x,y)\}\exp\left(-j\frac{2\pi}{\lambda z}(xx'+yy')\right)dxdy, \tag{2.17}$$

where

$$\begin{aligned} u(x,y) &= t(x,y)\times\exp\left(\frac{jk}{2z}(x^2+y^2)\right) \\ &= \exp\left(\frac{jk}{2z}(x^2+y^2)\right)\times\sum_{n=-\infty}^{\infty}A_n\exp\left(jn\pi\frac{x^2+y^2}{\rho^2}\right) \\ &= \sum_{n=-\infty}^{\infty}A_n\exp\left(j\pi(\frac{1}{\lambda z}+\frac{n}{\rho^2})(x^2+y^2)\right). \end{aligned} \tag{2.18}$$

Aside from multiplicative phase factors preceding the integral, Equation (2.17) is simply the Fourier transform of $u(x,y)(f_1(x,y)+f_2(x,y))$, evaluated at frequencies $(x'/\lambda z, y'/\lambda z)$. Let $\mathcal{F}$ denotes the Fourier transform. Then, Equation (2.17) can be expressed as

$$E(x',y') = \frac{\exp(jkz)\exp\left(\frac{jk}{2z}(x'^2+y'^2)\right)}{j\lambda z}[\mathcal{F}\{f_1(x,y)\}+\mathcal{F}\{f_2(x,y)\}]\otimes\mathcal{F}\{u(x,y)\}. \tag{2.19}$$

Here, the symbol $\otimes$ represents convolution operator. Using

$$\mathcal{F}\{f_1(x,y)\} = \exp\left(-j\frac{2\pi}{\lambda}\sin\theta_1\varepsilon\right)\delta\left(\frac{x'}{\lambda z}-\frac{\sin\theta_1}{\lambda},\frac{y'}{\lambda z}\right),$$

$$\mathcal{F}\{f_2(x,y)\} = \exp\left(j\frac{2\pi}{\lambda}\sin\theta_2\varepsilon\right)\delta\left(\frac{x'}{\lambda z}+\frac{\sin\theta_2}{\lambda},\frac{y'}{\lambda z}\right),$$

$$\mathcal{F}\{u(x,y)\} = \sum_{n=-\infty}^{\infty} \frac{jA_n}{1/\lambda z + n/\rho^2} \exp\left[\frac{-j\pi}{1/\lambda z + n/\rho^2}\left((\frac{x'}{\lambda z})^2 + (\frac{y'}{\lambda z})^2\right)\right],$$

where $\delta(x', y')$ represents a two-dimensional Dirac delta function, Equation (2.17) is re-expressed as,

$$E(\mathbf{r}) = \frac{\exp(jkz)\exp\left(\frac{jk}{2z}(x'^2 + y'^2)\right)}{j\lambda z} \times \left\{g_1(\mathbf{r})\exp\left(-j2\pi\frac{\sin\theta_1}{\lambda}\varepsilon\right) + g_2(\mathbf{r})\exp\left(j2\pi\frac{\sin\theta_2}{\lambda}\varepsilon\right)\right\} \tag{2.20}$$

where

$$\mathbf{r} = (x', y'),$$

$$g_1(\mathbf{r}) = \sum_{m=-\infty}^{\infty} \frac{jA_m}{1/\lambda z + m/\rho^2} \exp\left[\frac{-j\pi}{\lambda z + m(\lambda z/\rho)^2}\left|\mathbf{r} - \mathbf{r_1}\right|^2\right],$$

$$g_2(\mathbf{r}) = \sum_{n=-\infty}^{\infty} \frac{jA_n}{1/\lambda z + n/\rho^2} \exp\left[\frac{-j\pi}{\lambda z + n(\lambda z/\rho)^2}\left|\mathbf{r} - \mathbf{r_2}\right|^2\right],$$

$$\mathbf{r_1} = (z\sin\theta_1, 0),$$

$$\mathbf{r_2} = (-z\sin\theta_2, 0).$$

Then, the intensity distribution across the (x', y') plane is given by

$$I(\mathbf{r}) = E(\mathbf{r})E^*(\mathbf{r}) = \frac{1}{(\lambda z)^2}[g_1(\mathbf{r})^2 + g_2(\mathbf{r})^2 + 2\cos(\frac{2\pi}{\Lambda}\varepsilon)g_1(\mathbf{r})g_2(\mathbf{r})]. \tag{2.21}$$

The tramsmittance functions of $g_1(\mathbf{r})$ and $g_2(\mathbf{r})$ are similar to that of a Fresnel zone plate, so their focal lengths can be obtained as

$$F_m = \frac{m\lambda z^2}{\rho^2}, \tag{2.22}$$

assuming $z \gg \rho$. For a conventional zone plate that has $\rho^2 = \lambda f$, Equation (2.22) becomes

$$F_m = \frac{mz^2}{f}. \tag{2.23}$$

Equation (2.21) represents the interference irradiance distribution in the observation plane composed of two diffraction patterns of the Fresnel zone plate under illumination by two plane waves and the superposition of these patterns modulated by a periodic function of ε. The two diffraction patterns denoted by $g_1(\mathbf{r})^2$ and $g_2(\mathbf{r})^2$ will be called diffraction zone plates, and the third term are called moiré zone plates. The moiré zone plates are formed by the interference of two diffraction zone plates. They have multiple orders depending on the combination of m and n, and the first-order which has the highest irradiance, is located between the centers of two diffraction zone plates, $g_1(\mathbf{r})^2$ and $g_2(\mathbf{r})^2$. If $g_1(\mathbf{r})^2$ and $g_2(\mathbf{r})^2$ are located with a small separation of their centers, the interference patterns are dominated by linear fringes, not the moiré zone plates [16].

Let us examine the relationship of the irradiance across the (x', y') plane and the image grating characteristics. If intensity given by Eqn. (2.21) is integrated over a sample area on the (x', y') plane, the optical power is obtained and it is a cosine function of ε. The ε refers to the displacement of the Fresnel zone plate relative to an image grating that is phase-locked to (ξ, η) plane. In other words, the optical power measured over the (x', y') plane is a periodic function of the displacement of

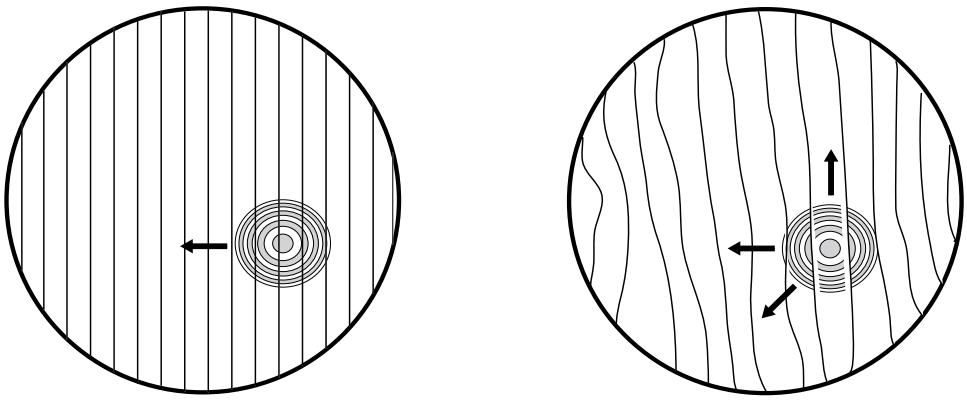

Figure 2-6: Image grating metrology using a Fresnel zone plate: (a) Image grating period measurement and (b) Image grating mapping

the Fresnel zone plate, and it has the same period as the image grating. Therefore, by scanning the Fresnel zone plate across the image grating, the image grating period can be obtained through the observation of the changes in optical power.

The phase of an image in the (ξ, η) plane is related to the image period by

$$\Lambda(\xi, \eta) = \frac{2\pi}{\left|\vec{\nabla}\phi\right|}, \tag{2.24}$$

where the symbol $\vec{\nabla}$ denotes the del operator given by $\vec{\nabla} = (\partial/\partial\xi, \partial/\partial\eta)$. Therefore, the distortion and local period of the image can be obtained directly with the knowledge of the image phase. In our case, the phase of the image grating in the (ξ, η) plane is

$$\phi(\xi, \eta) = \frac{2\pi}{\Lambda}\xi, \tag{2.25}$$

assuming two incident plane waves, and the phase of the optical power in the (x', y') plane is given by

$$\phi(\varepsilon) = \frac{2\pi}{\Lambda}\varepsilon. \tag{2.26}$$

Thus, one can find that the phase of an image grating through the measurement of the phase of the optical power by changing the relative phase between the two

beams. The distortion and orientation of an image grating can also be characterized by scanning the Fresnel zone plate under the image grating in all directions (Fig. 2-6).

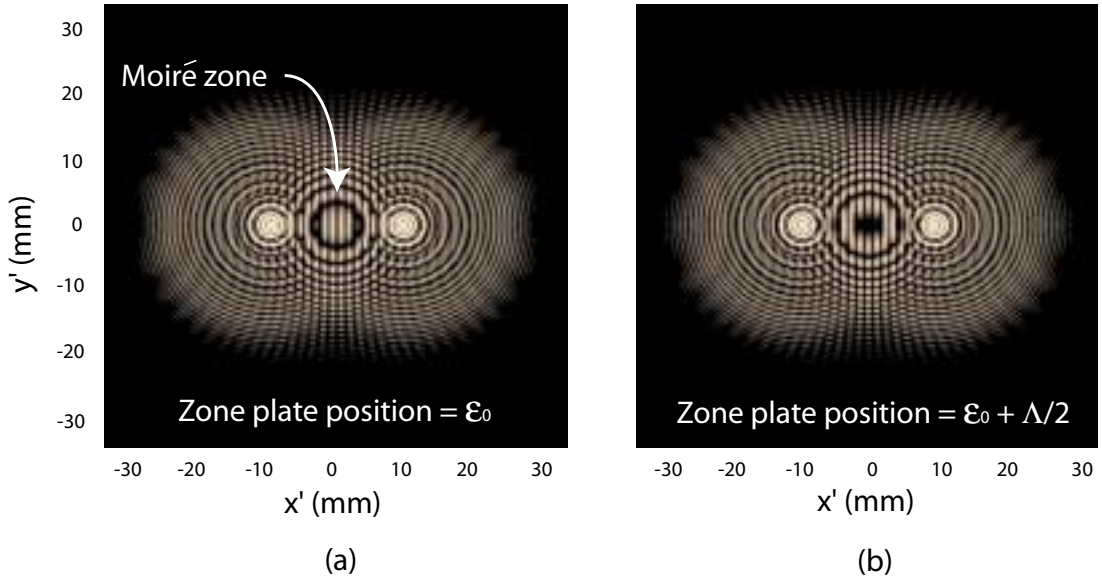

Figure 2-7: Simulated diffraction pattern of two plane waves by a Fresnel zone plate: λ=400 nm; z=10 cm; number of zones=12; minimum zone width=1 μm.

Figure 2-7 shows numerical simulation results for the irradiance distribution produced by an image grating transmitted through a Fresnel zone plate. Note that the phase of the first-order moiré zone plates, shown in Fig. 2-7(a), changes by π as the Fresnel zone plate is displaced by one half of the image grating period, as shown in Fig. 2-7(b). The first-order moiré zone plate is the one that can be found by setting $m = n$ in the tramsittance function, $g_1(\mathbf{r})g_2(\mathbf{r})$.

2.3 Range of image grating period

Suppose that a Fresnel zone plate is to be used for characterizing an image grating with a period that can be varied during the operation. Obviously, the Fresnel zone plate can be used as long as the interference of the diffraction waves occurs. Of interest are the properties of the Fresnel zone plate that limit the range of image grating periods that can be measured for the given Fresnel zone plate? In this section, I study the diffraction of two plane waves by a Fresnel zone plate in a different way

to obtain useful expressions that define the range of image grating period measurable for a given zone plate.

As discussed, the image grating metrology using a Fresnel zone plate essentially uses interference of diffracted waves by a Fresnel zone plate. The diffracted waves of a plane wave are composed of the zeroth order plane wave propagating with the same wave vector as the incident wave and the higher order spherical waves with different focal points.

Figure 2-8 illustrates the diffraction of a plane wave by a Fresnel zone plate, where only the $\pm$1st order diffraction waves are shown. The zeroth and the higher order diffraction waves are omitted for clarity. If the other plane wave is also illuminated on the Fresnel zone plate to produce an image grating, it is diffracted, forming moiré zone plates in the observation plane because of the interference of the spherical waves (Fig. 2-9).

In order for the moiré zone plates to be formed with enough power for measurement, the $\pm$1st order spherical waves should be superimposed in the observation plane. Figure 2-10 (a) depicts the case where the moiré zone plates can be observed. However, as the incident angle of the plane waves increases and the image grating period shrinks, the -1st order spherical waves will no longer be overlapped, as shown in Fig. 2-10 (b). This condition can be found using the grating equation [18]. Assume that a Fresnel zone plate has a minimum zone width of δr, and two plane waves have an incident angle of θ_i. Since the outer zones of the Fresnel zone plate are very fine, they can be regarded as a localized grating of period $d = 2\delta r$. Then, the -1st order spherical waves will not interfere with that of the other plane wave if the first-order diffraction angle is equal to the incident angle, or

$$d \sin\theta|_{\theta=\theta_i} = \lambda. \tag{2.27}$$

The minimum image grating period, for the incident angle found above, is obtained as

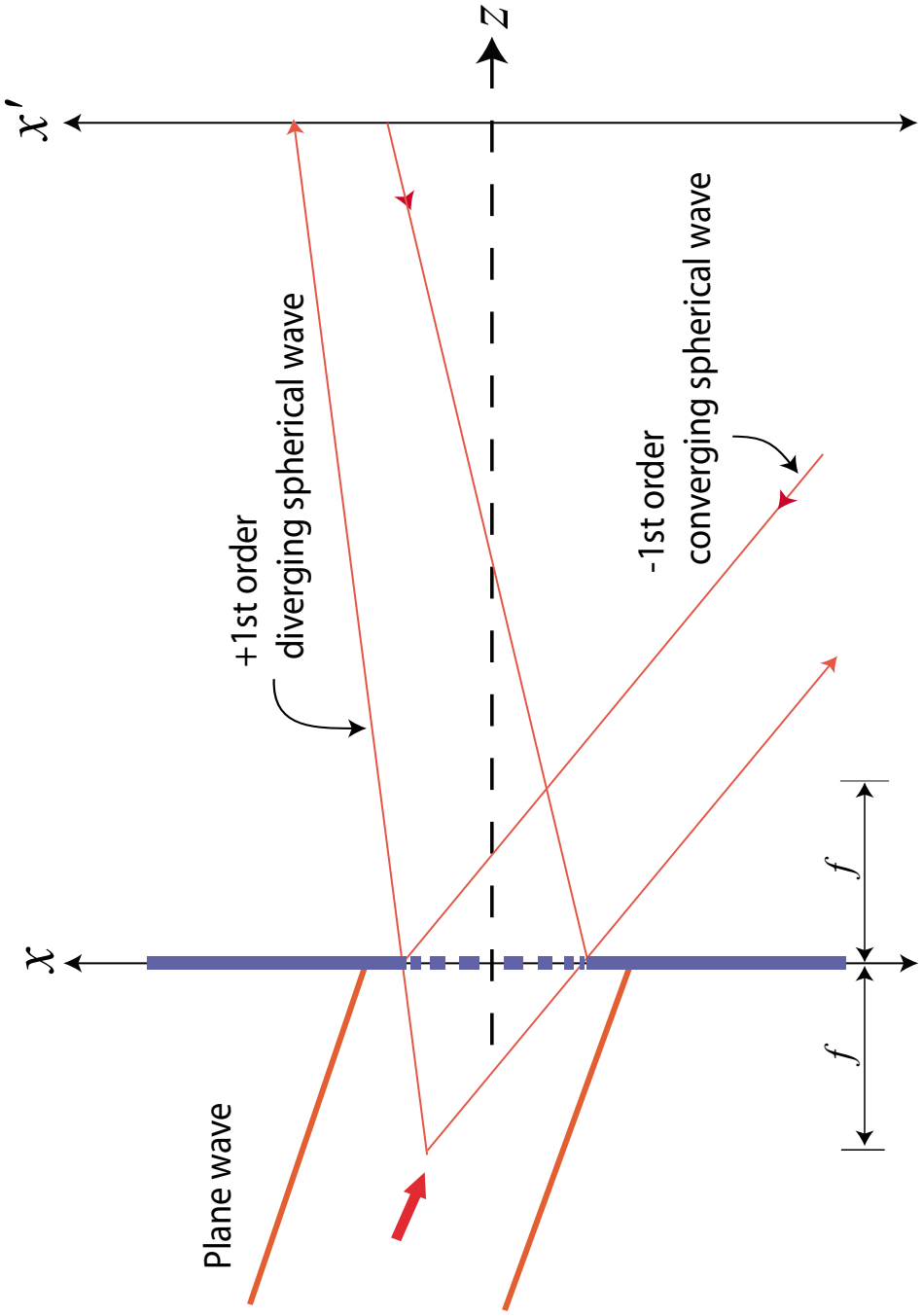

Figure 2-8: Diffraction of a plane wave by a Fresnel zone plate. The plane wave is diffracted into multiple orders: the zeroth order plane wave and the higher order spherical waves. In the Figure, the plane wave is incident on the Fresnel zone plate with an incident angle. Only the ±1st spherical waves are shown for clarity.

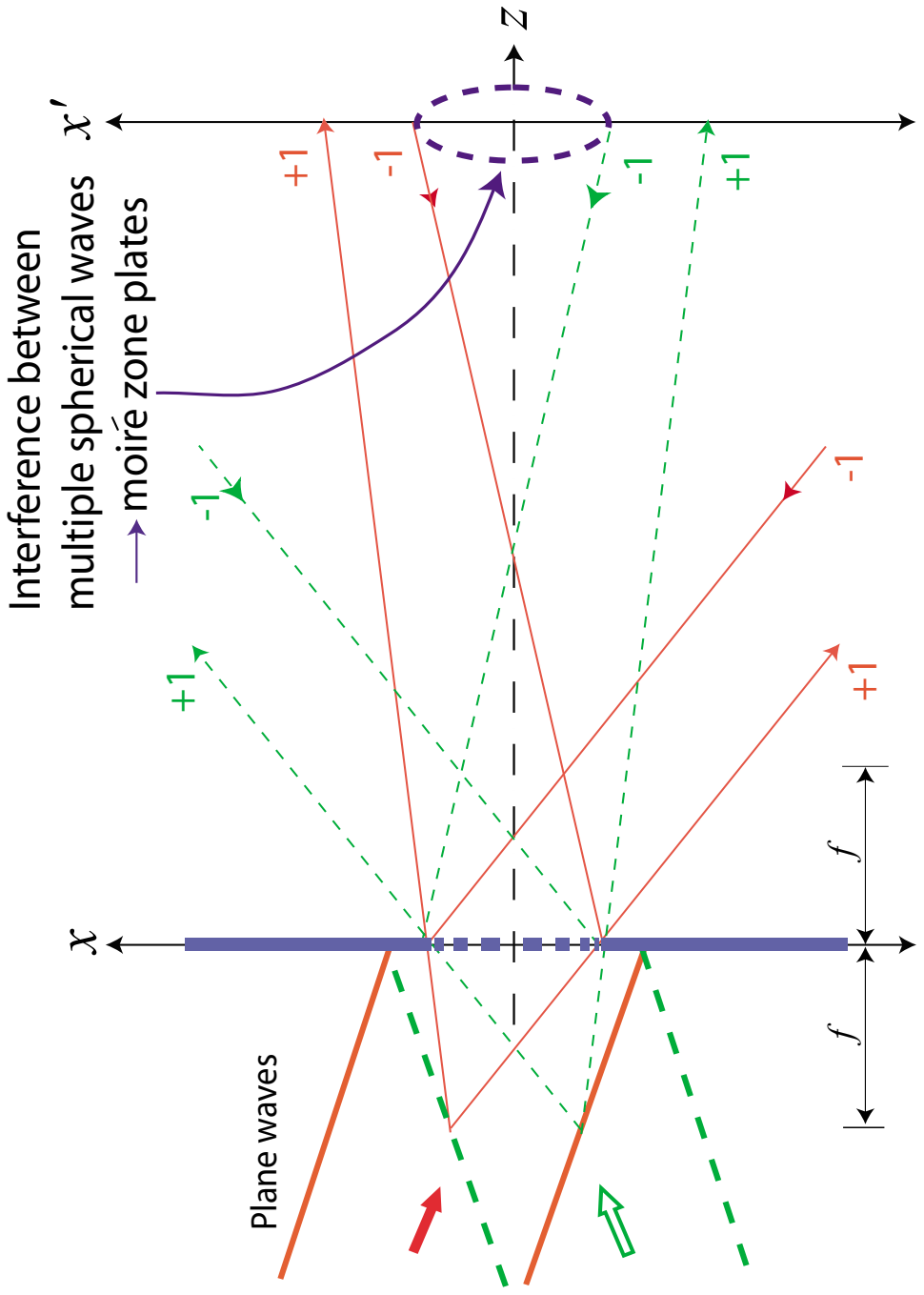

Figure 2-9: Diffraction of two plane waves by a Fresnel zone plate. Interference of two plane waves produces an image grating in the (x, y) plane. The two plane waves are diffracted by the Fresnel zone plate, and the interference of their multiple diffraction orders are observed in the (x', y') plane. The moiré zone plates are formed in the region indicated with the dashed lines. Only the $\pm$1st spherical waves are shown for clarity.

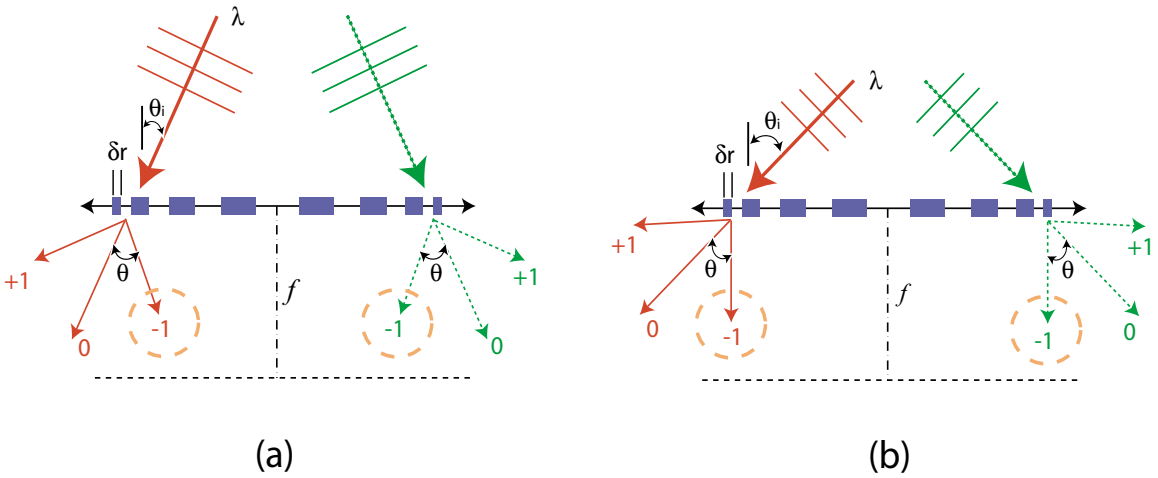

Figure 2-10: Diffraction of two plane wave by a Fresnel zone plate. The -1st order diffraction waves, which are converging spherical waves, are superimposed in the observation plane, forming moiré zone plates (a), but as the incident angle is larger and reaches to the N.A. of the Fresnel zone plate, they will no longer overlapped, as shown in (b).

$$\Lambda_{min} = \frac{\lambda}{2\sin\theta_i} = \delta r. \tag{2.28}$$

Hence, the Λ_{min} depends on the minimum zone width, δr of the Fresnel zone plate. The numerical aperture (N.A.) of a Fresnel zone plate is also evaluated as,

$$N.A. = \frac{\lambda}{2\delta r} = \sin\theta_i. \tag{2.29}$$

It shows that the N.A. of a Fresnel zone plate defines the limiting incident angle for the diffraction zone plates to be superimposed in the observation plane. Figure 2-11 shows the case where the incident angle is equal to the N.A. of the Fresnel zone plate. The wavelength of the beam is 400 nm and the Fresnel zone plate has a minimum zone width of 1 μm, which corresponds to 0.2 in numerical aperture. The moiré zone plates are not seen because the diffraction zone plates are not superimposed.

Thus far, the analysis has been made based on two important assumptions: (1) the paraxial approximation and (2) the beam has a shorter wavelength than the minimum local period of a Fresnel zone plate. The assumption (1) says that the incident angle denoted by θ_i is small, so that $\sin\theta_i \simeq \theta_i$. The second assumption is that the incident

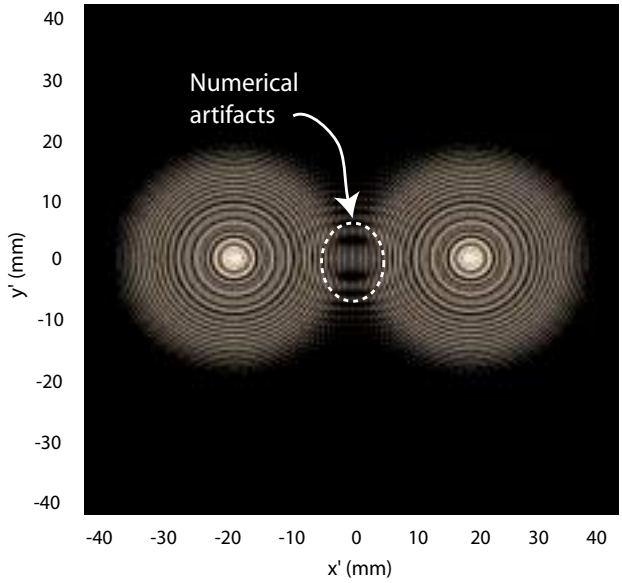

Figure 2-11: Simulated the case in which incident angle equals to the N.A. of the Fresnel zone plate. The diffraction zone plates are not overlapped, so the moiré zone plates are not observed.

waves on a Fresnel zone plate are all diffracted by each zone. In fact, the second assumption can be easily broken. Consider the case depicted in Fig. 2-12. Here, the Fresnel zone plate is assumed to have smaller localized grating period of $2\delta r$ in the outer zones such that

$$\sin\theta = \frac{\lambda}{2\delta r} - \sin\theta_i > 1. \tag{2.30}$$

It is the case that the incident wave is reflected by the localized grating composed of the outer zones. Still, the moiré zone plates can be formed by the interference of the waves diffracted by the inner zones, which have larger period. However, optical power decrease of the moiré zone plates is expected because some portion of the incident beam is reflected, or the effective size of the Fresnel zone plate is decreased.

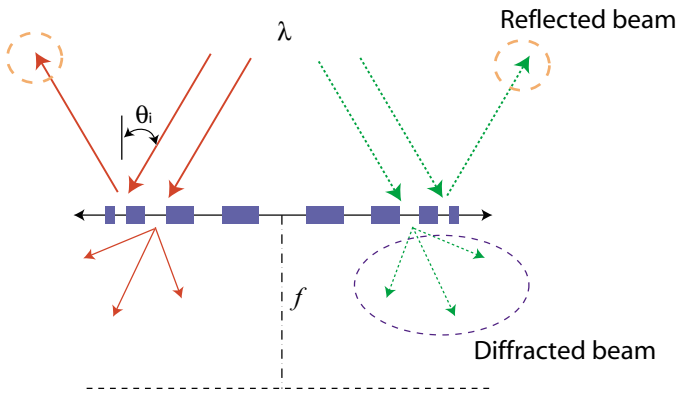

Figure 2-12: Diffraction of two plane wave by a high N.A. Fresnel zone plate. The incident wave is not diffracted by the local grating composed of the outer zones, since its period is smaller than the wavelength of the incident wave. However, the moiré zone plates are still formed because of the interference of the diffracted waves by the inner zones.

2.4 Contrast fluctuations vs. Image grating period

The Nanoruler, a prototype system of the SBIL, is expected to be capable of patterning linear or curved chirped gratings. It can be achieved by varying the image grating period and rotating the laser beams during the operation. Therefore, the image grating metrology needs to be applicable for a wide range of grating periods, regardless of changes in incident angle. To characterize an image grating accurately, it is necessary to have sufficient contrast in optical power fluctuations because the accurate measurement of the image grating characteristics critically depends on the determination of signal properties, i.e., peaks and valleys. This section is dedicated to examine the effects of varying image grating period on the capability of the image grating metrology using a Fresnel zone plate in terms of contrast fluctuations.

Assume that the incident angles of two plane waves are the same, $\theta = \theta_1 = \theta_2$, for simplicity. Then, Equation (2.21) can be expressed as

$$I(\mathbf{r}) = \frac{1}{(\lambda z)^2}\left[g(\mathbf{r}-\mathbf{r}_0)^2 + g(\mathbf{r}+\mathbf{r}_0)^2 + 2\cos(\phi)g(\mathbf{r}-\mathbf{r}_0)g(\mathbf{r}+\mathbf{r}_0)\right], \qquad (2.31)$$

where

$$g(\mathbf{r}) = \sum_{n=-\infty}^{\infty} \frac{jA_n}{1/\lambda z + n/\rho^2} \exp\left[\frac{-j\pi}{\lambda z + n(\lambda z/\rho)^2} |\mathbf{r}|^2\right],$$

$$\mathbf{r_0} = (z \sin\theta, 0) = (\frac{\lambda z}{2\Lambda}, 0),$$

and

$$\phi = \frac{2\pi}{\Lambda}\varepsilon.$$

Here, $\Lambda = \lambda/2\sin\theta$ is used, and $g(\mathbf{r})$ is a circularly symmetric chirped function similar to the amplitude transmittance of the Fresnel zone plate.

If the intensity distribution given by Eqn. (2.31) is integrated over the innermost zone of the first-order moiré zone plate indicated in Fig. 2-7, the power is evaluated as

$$\begin{aligned} P(\Lambda) &= \frac{1}{(\lambda z)^2}\left[\int\int_A \left\{g(\mathbf{r}-\mathbf{r_0})^2 + g(\mathbf{r}+\mathbf{r_0})^2\right\} dA + 2\int\int_A g(\mathbf{r}-\mathbf{r_0})g(\mathbf{r}+\mathbf{r_0})dA \ \cos\phi\right] \\ &= \frac{1}{(\lambda z)^2}\left[D_A(\Lambda) + N_A(\Lambda) \ \cos\phi\right], \end{aligned} \tag{2.32}$$

and the contrast can then be defined by

$$C_A(\Lambda) = \left|\frac{P_{max} - P_{min}}{P_{max} + P_{min}}\right| = \left|\frac{N_A(\Lambda)}{D_A(\Lambda)}\right|. \tag{2.33}$$

The innermost zone of the first-order moiré zone plate is used to calculate optical power because it maximizes the signal contrast. Suppose that the innermost zone is bright. If one increases the sample area to include the second zone that is dark, the innermost zone will turn to be dark and the second zone will be bright as a Fresnel zone plate moves by one half of the image grating period. The optical power is the sum of intensity over the sample area, so one cannot expect significant changes in optical power, though the Fresnel zone plate moves. The inclusion of more zones in

the sample area will reduce the contrast of power fluctuations.

Note that the contrast is expressed as a function of image grating period, Λ, as shown in Eqn. 3.28. It is unity if $g(\mathbf{r}-\mathbf{r_0}) = \pm g(\mathbf{r}+\mathbf{r_0})$ over the innermost zone of the first-order moiré zone plate. However, since $g(\mathbf{r})$ is a quadratic chirped function, $g(\mathbf{r}-\mathbf{r_0})$ cannot be equal to $\pm g(\mathbf{r}-\mathbf{r_0})$ over the region centered at the origin for $\theta \neq 0$, but they are mirror-symmetric relative to the z axis. Thus, the contrast cannot be unity if the incident angle is not zero.

Since linear fringes dominate the interference pattern for small separation between $g(\mathbf{r}-\mathbf{r_0})$ and $g(\mathbf{r}+\mathbf{r_0})$, the separation is assumed to be large enough, so that the moiré zone plates can be observed. Then, the sample region defined above covers many outer zones of $g(\mathbf{r}-\mathbf{r_0})$ and $g(\mathbf{r}+\mathbf{r_0})$, so it can be true that $D_A(\Lambda)$, essentially a sum of the power of two diffraction patterns, is not much affected by the changes in Λ. In other words, the in-and-out motion of the fine outer zones in the integral region due to the changes in image grating period does not greatly affect $D_A(\Lambda)$ over the range of Λ considered, so that

$$\frac{dD_A(\Lambda)/d\Lambda}{D_A(\Lambda)} \ll 1. \tag{2.34}$$

Hence, the contrast can be thought to be dependent only on $N_A(\Lambda)$. Some readers might be interested in exact expressions for image grating periods at which the contrast takes extreme values, i.e., maxima and minima. It must be true that

$$\frac{dC_A(\Lambda)}{d\Lambda} = \left| \frac{\frac{dN_A(\Lambda)}{d\Lambda} D_A(\Lambda) - N_A(\Lambda)\frac{dD_A(\Lambda)}{d\Lambda}}{D_A(\Lambda)^2} \right| = 0, \tag{2.35}$$

for the image grating periods where the contrast has extreme values.
Since the second term in the numerator of Eqn. (2.35) is negligible, and $D_A(\Lambda)$ cannot be zero in the innermost zone of the first moiré zone plate, $dN_A(\Lambda)/d\Lambda = 0$ is obtained. To evaluate $N_A(\Lambda)$,

$g(\mathbf{r}-\mathbf{r_0})g(\mathbf{r}+\mathbf{r_0})$

$$= \sum_{m=-\infty}^{\infty} \frac{jA_m}{1/\lambda z + m/\rho^2} \exp\left[\frac{-j\pi \left|\mathbf{r}-\mathbf{r_0}\right|^2}{\lambda z + m(\lambda z/\rho)^2}\right] \sum_{n=-\infty}^{\infty} \frac{jA_n}{1/\lambda z + n/\rho^2} \exp\left[\frac{-j\pi \left|\mathbf{r}+\mathbf{r_0}\right|^2}{\lambda z + n(\lambda z/\rho)^2}\right]$$

$$= -\sum_{n=-\infty}^{\infty} \left(\frac{A_n}{1/\lambda z + n/\rho^2}\right)^2 \exp\left[\frac{-j2\pi\left(\left|\mathbf{r}\right|^2 + \left|\mathbf{r_0}\right|^2\right)}{\lambda z + n(\lambda z/\rho)^2}\right] \tag{2.36}$$

Here, $m = n$ is used because the first order moiré zone plate centered at the origin is being considered [16]. Then,

$$\begin{aligned} N_A(\Lambda) &= \int\int_A 2g(\mathbf{r}-\mathbf{r_0})g(\mathbf{r}+\mathbf{r_0})dA \\ &= -2\int\int_A \left\{\sum_{n=-\infty}^{\infty} \left(\frac{A_n}{1/\lambda z + n/\rho^2}\right)^2 \exp\left[\frac{-j2\pi\left(\left|\mathbf{r}\right|^2 + \left|\mathbf{r_0}\right|^2\right)}{\lambda z + n(\lambda z/\rho)^2}\right]\right\} dA \\ &= -2\sum_{n=-\infty}^{\infty} \left(\frac{A_n}{1/\lambda z + n/\rho^2}\right)^2 \exp\left[\frac{-j2\pi\left|\mathbf{r_0}\right|^2}{\lambda z + n(\lambda z/\rho)^2}\right] \int\int_A \exp\left[\frac{-j2\pi\left|\mathbf{r}\right|^2}{\lambda z + n(\lambda z/\rho)^2}\right] dA \\ &= \sum_{n=-\infty}^{\infty} B_n \exp\left[\frac{-j2\pi\left|\mathbf{r_0}\right|^2}{\lambda z + n(\lambda z/\rho)^2}\right], \end{aligned} \tag{2.37}$$

where

$$B_n = -2\left(\frac{A_n}{1/\lambda z + n/\rho^2}\right)^2 \int\int_A \exp\left[\frac{-j2\pi\left|\mathbf{r}\right|^2}{\lambda z + n(\lambda z/\rho)^2}\right] dA.$$

Equation (2.37) can be further simplified as

$$N_A(\Lambda) = \sum_{n=-\infty}^{\infty} B_n \exp\left[\frac{-j\beta_n}{\Lambda^2}\right]. \tag{2.38}$$

using $\mathbf{r_0} = (\lambda z/2\Lambda, 0)$, and

$$\beta_n = \frac{\pi}{2\left(1/\lambda z + n/\rho^2\right)}.$$

Equation (2.37) reveals that $N_A(\Lambda)$ is a chirped function of Λ for a given Fresnel zone plate and the free-space propagation distance z. In other words, the contrast is also a function of the free-space distance z and the properties of the Fresnel zone plate such as the innermost zone radius ρ and the numerical aperture. High frequency contrast fluctuations are predicted for small image grating periods and lower frequency

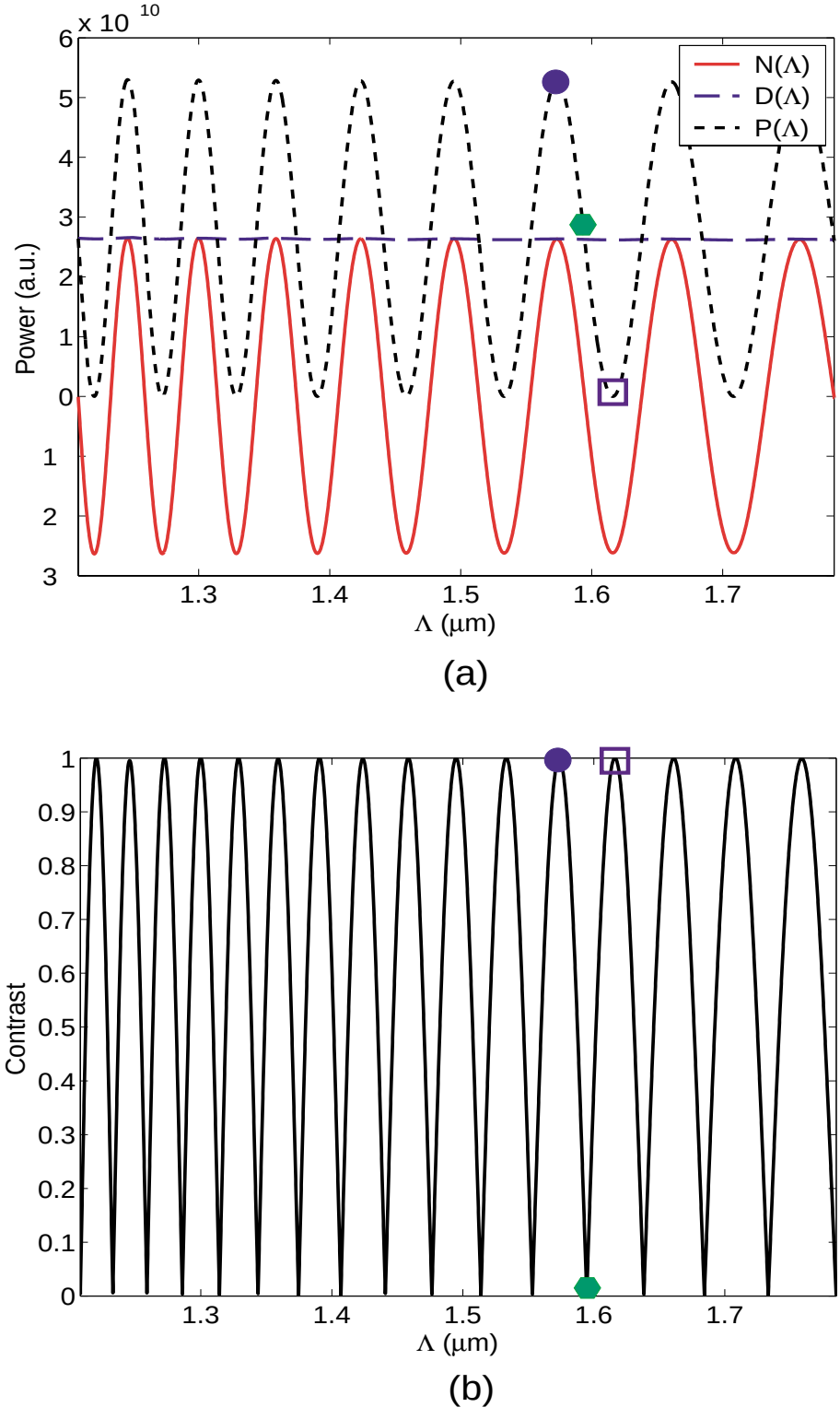

Figure 2-13: Three components, $N(\Lambda)$, $D(\Lambda)$, and $P(\Lambda)$ are shown in (a), and contrast fluctuations of the innermost zone of the first-order moiré zone plate with varying image grating period is shown in (b). For reference, three cases are indicated to show that the contrast takes maximum values as the $P(\Lambda)$ is either maximum or minimum.

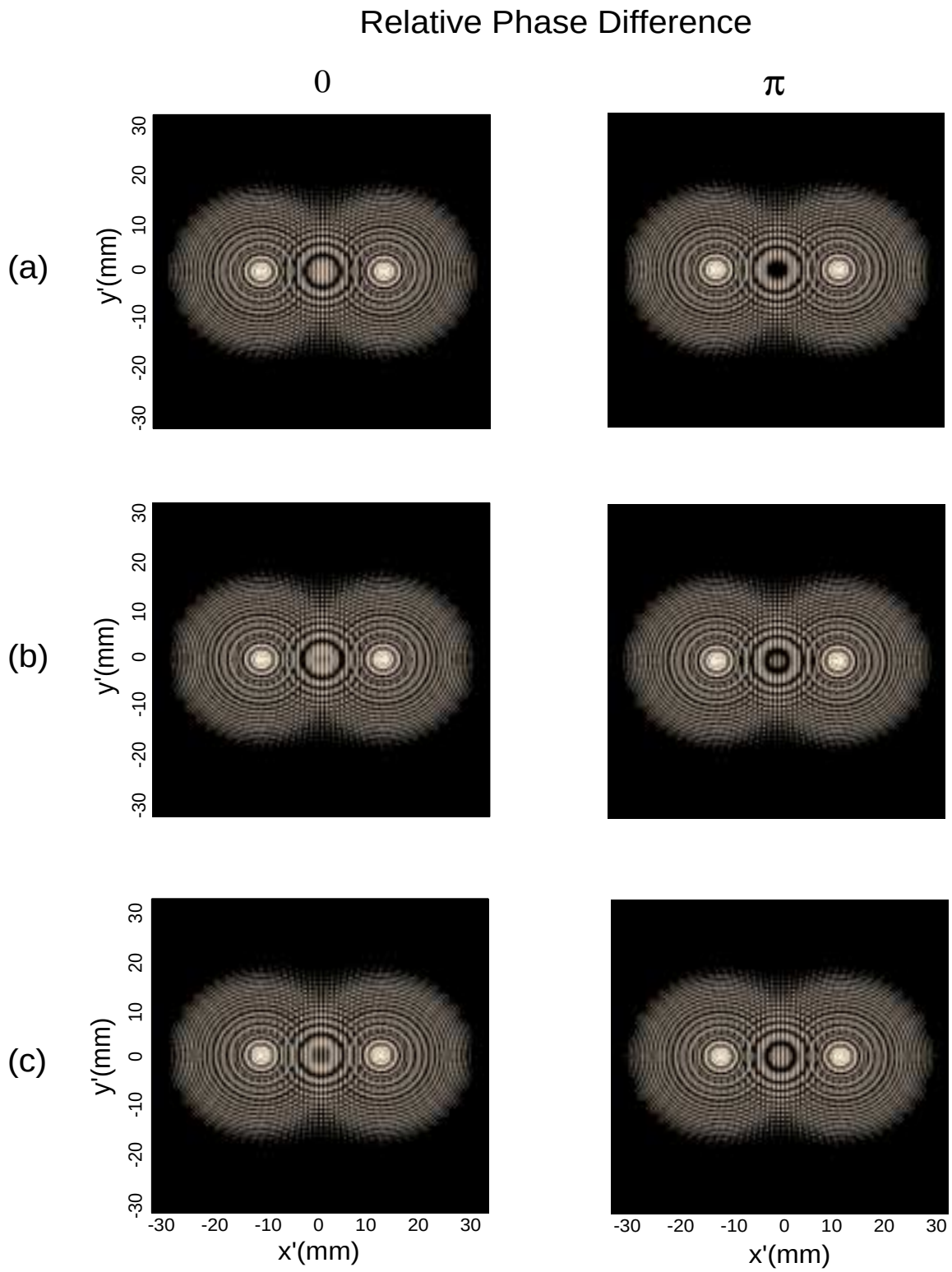

Figure 2-14: Simulated optical power variations of the innermost zone of the first-order moiré zone plate as the relative phase of the diffraction zone plates changes. The sample area has a radius of 1.5 mm. (a) $\Lambda = 1.5735$ μm, Contrast = 0.997, (b) $\Lambda = 1.5946$ μm, Contrast = 0.004, (b) $\Lambda = 1.6161$ μm, Contrast = 0.991.

fluctuations for large image grating periods.

The simulation confirms the prediction (Fig. 2-13). I used a beam with a wavelength of 400 nm, and the Fresnel zone plate is assumed to have 14 zones and an innermost zone radius of 8 μm. The free-space propagation distance is 10 cm. The circular area with a radius of 1.5 mm in the observation plane (x', y') is used to sample the innermost zone of the first-order moiré zone plate for power calculation. As shown, $D(\Lambda)$ doesn't show significant power variations, whereas $N(\Lambda)$ fluctuates greatly by changes in image grating period. A lot of contrast fluctuations are observed for small image grating periods. I indicated three cases in Fig. 2-13: two maxima and one minimum. Note that the contrast takes maximum values when the power over the sample region is either maximum or minimum. As for the contrast minimum, it is easy to understand since the contrast takes a value of zero when the $N(\Lambda)$ is zero.

Figure 2-14 clearly shows the relationship of optical power in the sample area and the contrast. The three cases indicated in Fig. 2-13 are shown. The high contrast is obtained if the optical power over the sample area is maximum or minimum as the relative phase difference of diffraction zone plates is zero. If there are dark and bright regions in the sample area, one cannot expect significant power fluctuations, though the relative phase difference changes by π because the bright region will turn to be dark and the dark one will be bright, not giving significant power variations than before.

Chapter 3

Experiment

In order for SBIL to succeed in fabricating large gratings with nanometer level phase distortions, it is critical that the stage step over by an integer number of image periods between subsequent scans. In the current Nanoruler setup, a specially designed rectangular beamsplitter is mounted on the stage to measure the image grating period to the part-per-million (ppm) level (Fig. 3-1). However, the beamsplitter scheme cannot be applicable when the beams rotate and vary incident angles, which is necessary for the next-generation Nanoruler.

Using a Fresnel zone plate, image grating periods have been measured in a homodyne and a heterodyne scheme. As for the homodyne case, a simple Mach-Zehnder interferometry was set up using a HeNe laser ($\lambda = 632.8$ nm) and an amplitude Fresnel zone plate. I measured the optical power transmitted through the amplitude Fresnel zone plate as the zone plate moved under the image grating. In the heterodyne setup, a phase zone plate was installed in the current Nanoruler that uses a UV laser ($\lambda =$ 351.1 nm) and is configured to produce gratings of nominal period 400 nm. The image grating period was obtained by the phase variations of the signal transmitted through the zone plate. Contrast variations of optical power by changes in image periods has also been demonstrated. Using the same experimental setup of the homodyne case and a phase zone plate, contrast variation was measured.

The Fresnel zone plates used in the experiments were all fabricated by the Lawrence Berkeley National Laboratory (LBNL) *Nanowriter*. The *Nanowriter* is a high resolu-

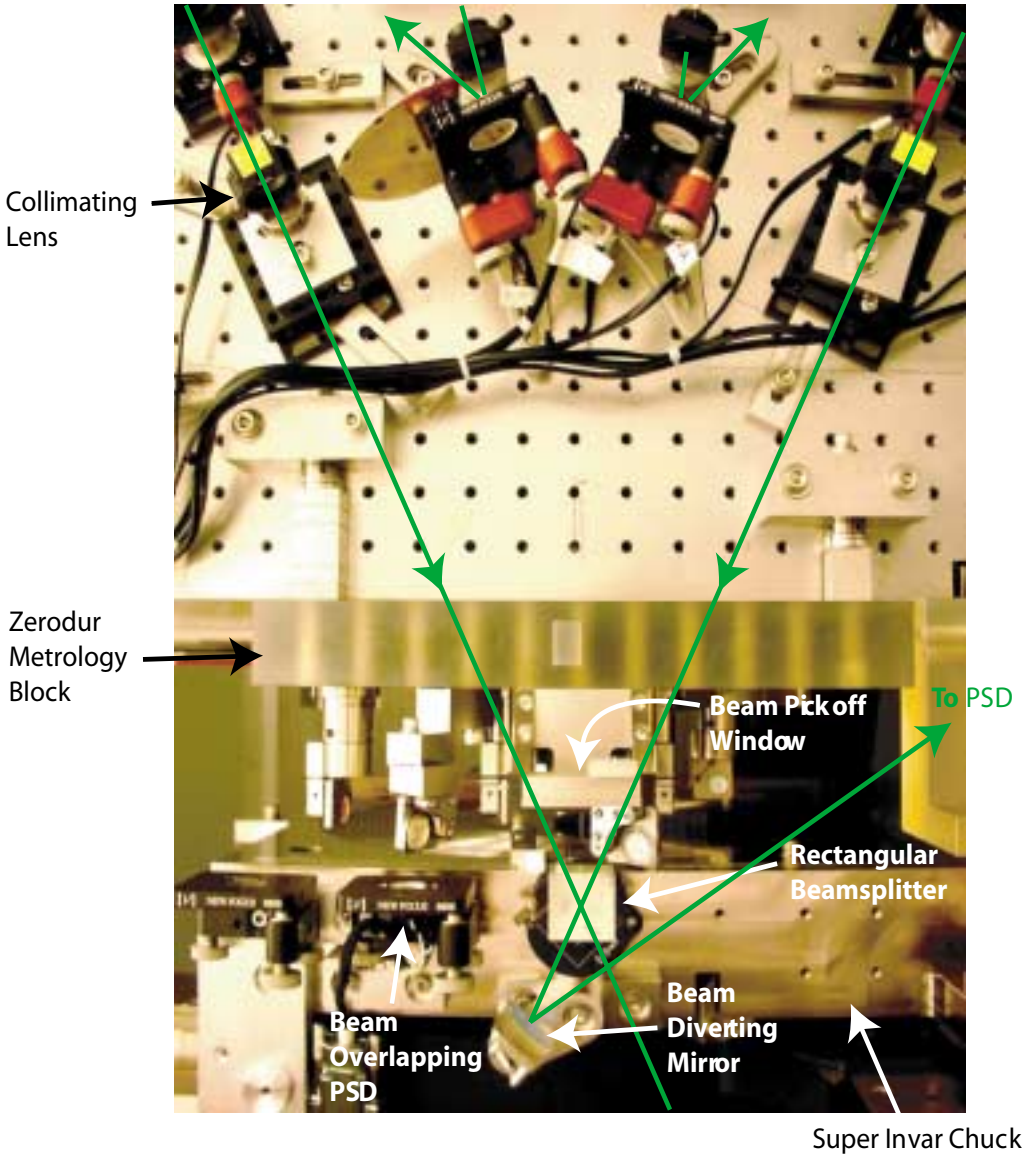

Figure 3-1: Period measurement system of the Nanoruler. Two beams interfere at the interface of the rectangular beamsplitter, and the mirror diverts the interference signal to the position sensing detector.

tion electron beam lithography tool, which has a placement fidelity of 5 nm in a 131 μm field [23]. It has a spot size of 5-8 nm, and for our experments, used a spot size of 8 nm.

3.1 Homodyne period measurement

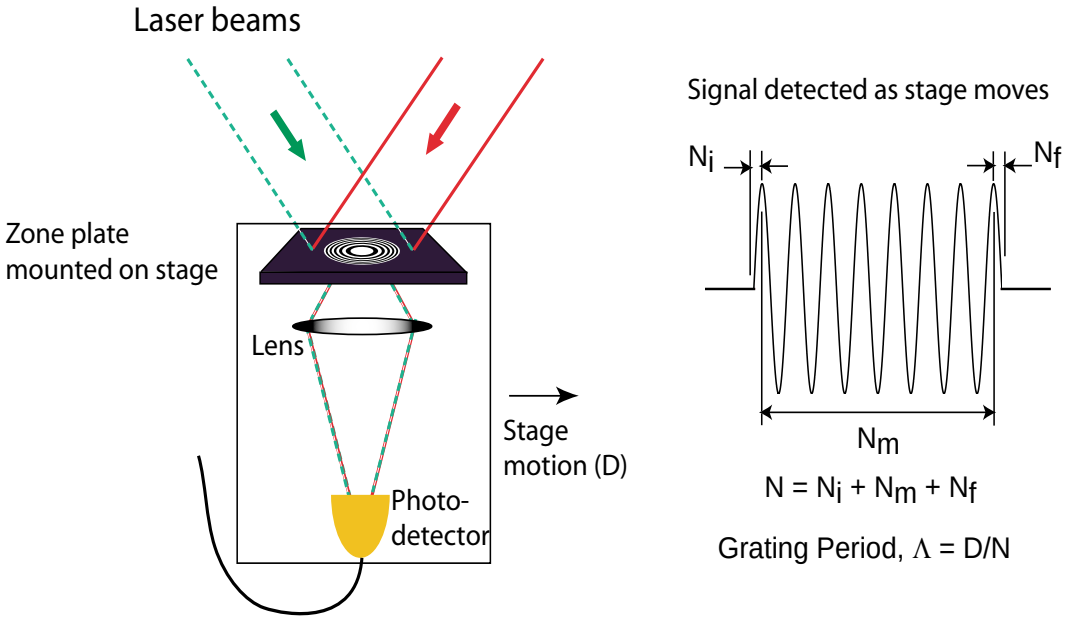

Figure 3-2: Homodyne period measurement concept.

The homodyne interferometry method uses two coherent laser beams with the same temporal frequency. Therefore, the interference pattern between two beams is a standing wave pattern called an image grating, so, in ideal case, the image grating is stabilized in the space. Figure 3-2 shows the concept of the homodyne image grating period measurement. The zone plate moves across the interference fringe lines, so the optical power transmitted through the zone plate varies sinusoidally with the same period of the image grating period. Then, the image grating period can be derived by

$$\Lambda = \frac{D}{N}, \tag{3.1}$$

where D is the distance traveled by the stage, and N is the total number of oscilla-

tions. Therefore, in the homodyne scheme, the accurate detection of the number of oscillations and the measurement of the displacement of the zone plate are crucial for accurate measurement of image period.

3.1.1 Oscillation counting algorithm

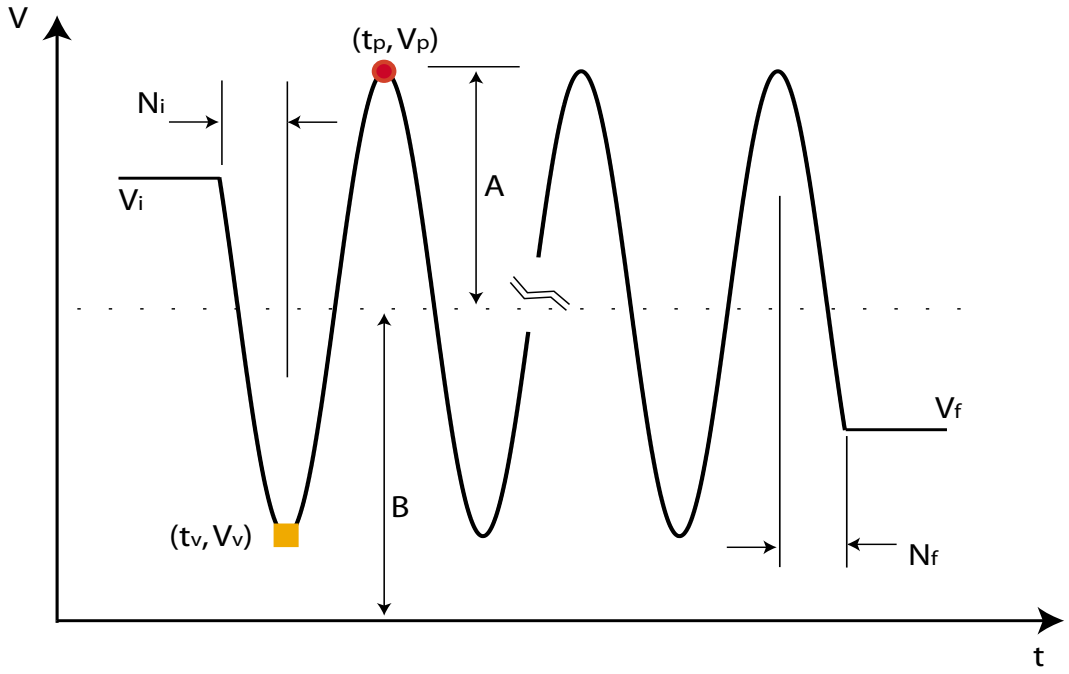

Figure 3-3: An example of optical power signal measured at a photodiode.

Figure 3-3 shows a schematic of the optical power measured at a photodiode as the stage moves. It is different from that described in Ref. [19], which has a Gaussian intensity envelope. The beamsplitter scheme results in a Gaussian intensity envelope, since the transmitted and reflected beams become mis-aligned as the beamsplitter moves across the image grating. However, in our case, it does not pose a problem because the small zone plate moves near the centroid of the Gaussian-enveloped image grating. The photodiode voltage readout before the stage motion is V_i, and the final voltage, when the stage completes the motion, is represented by V_f. The number of oscillations is the sum of three terms: the fractional number of oscillations at the beginning (N_i) and the end (N_f), and the completed cycles N_m. In order to accurately count the number of oscillations (N), the oscillation counting algorithm

has been implemented using the MATLAB, and the relevant codes are included in Appendix D. Chen also implemented the oscillation counting algorithm using the LabView [19].

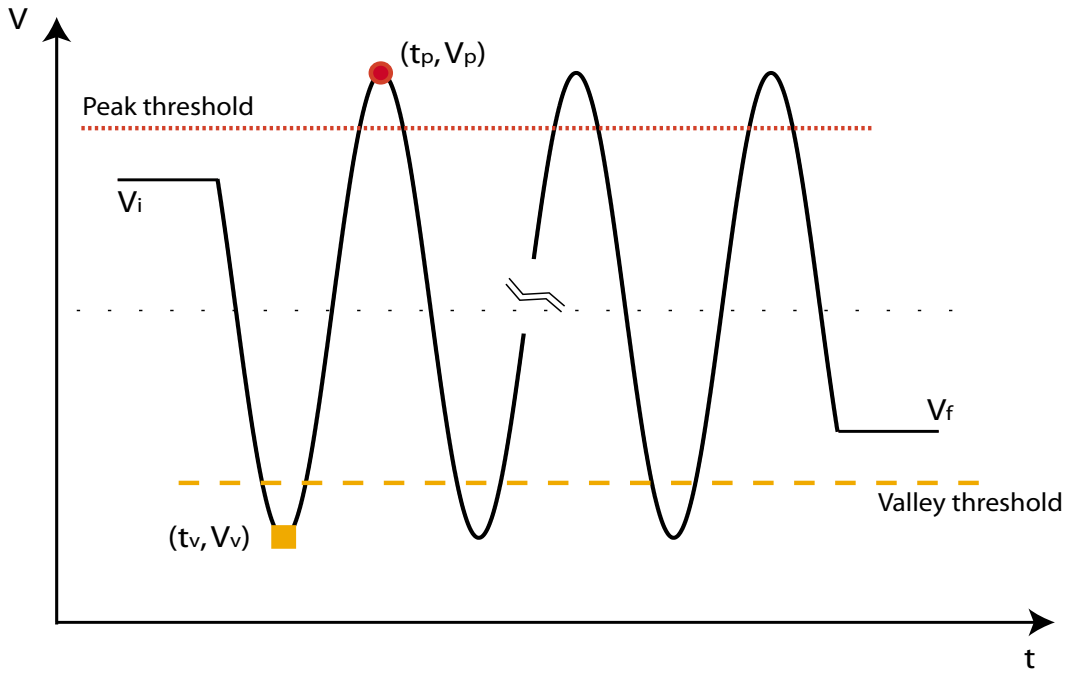

Figure 3-4: Signal and thresholds to detect peaks and valleys.

Figure 3-5 depicts three cases that may be observed at the output of a photodiode during the period measurement. As illustrated, the number of completed cycles (N_m) can be derived easily by the numbers of peaks (n_p) and valleys (n_v) present in the signal. To find the numbers of peaks and valleys, and their locations and values, I define the thresholds as depicted in Fig. 3-4. If the signal begins below the threshold value, exceed the threshold at some location, and then return to a value below, one peak exists in that range. The location and value of the peak are obtained by fitting the data in the range as a second order polynomial and taking its derivative to find its location and value. In the same way, the location and value of the valleys are found. The peak and valley detection procedure is implemented in PVdetector.m in Appendix D.

The fractional number of oscillations is obtained using a sinusoidal function of t to fit the signal in the beginning and the end. Assume a sine function defined by

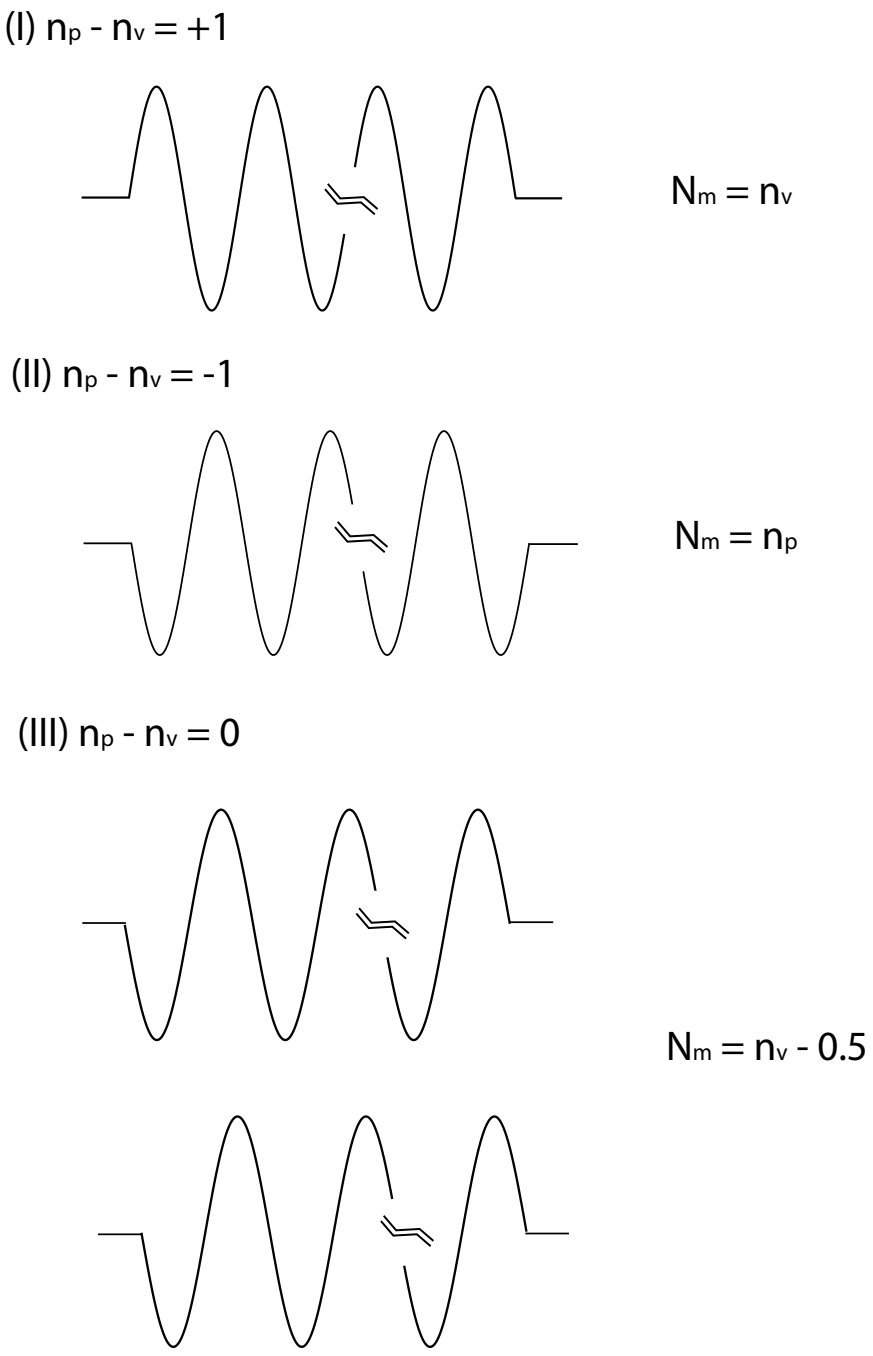

Figure 3-5: Three cases that may be observed at a photodiode. Based on the numbers of peaks (n_p) and valleys (n_v), the number of completed cycles, N_m, can be deduced.

$$V(t) = A\sin(Ct + D) + B. \tag{3.2}$$

It has four unknowns, and they can be found using the mean values of the peaks and valleys, and the initial (or final) peak or valley location and value. The coefficients A and B are given by

$$A = \frac{V_p - V_v}{2}, \tag{3.3}$$

$$B = \frac{V_p + V_v}{2}, \tag{3.4}$$

where V_p and V_v are the mean peak and valley values, respectively, and the constants C and D can also be found using the location and value of the initial (or final) peak or valley. Then, the fractional number of oscillations are calculated by

$$N_i = \frac{1}{4} - \frac{1}{2\pi}\left|\arcsin\left(\frac{V_i - B}{A}\right)\right|, \tag{3.5}$$

$$N_f = \frac{1}{4} - \frac{1}{2\pi}\left|\arcsin\left(\frac{V_f - B}{A}\right)\right|. \tag{3.6}$$

Finally, the number of oscillations are obtained by summing N_i, N_f, and N_m.

Carl Chen has modeled the errors associated with the determination of the number of oscillations [19]. Using his mathematical error models and knowing that the total number of cycles $N = N_i + N_m + N_f$, the error variance is,

$$\Delta N^2 = \Delta N_i^2 + \Delta N_f^2. \tag{3.7}$$

One can easily understand that $\Delta N_m^2 = 0$, since there is no ambiguity in getting N_m algorithmatically. If I use the notation "$*$" to denote either "i" or "f" , the ΔN_*^2 can be expressed by differentiating Eqn. (3.5) or (3.6) with respect to V_*, A, and B:

$$\Delta N_*^2 = \left(\frac{\Delta V_*}{2\pi A\sqrt{1-\frac{(V_*-B)^2}{A^2}}}\right)^2 + \left(\frac{\Delta B}{2\pi A\sqrt{1-\frac{(V_*-B)^2}{A^2}}}\right)^2 + \left(\frac{(V_*-B)\Delta A}{2\pi A^2\sqrt{1-\frac{(V_*-B)^2}{A^2}}}\right)^2, \tag{3.8}$$

where

$$\Delta B^2 = \Delta A^2 = \left(\frac{1}{2}\Delta V_p^2\right)^2 + \left(\frac{1}{2}\Delta V_v^2\right)^2. \tag{3.9}$$

Equation 3.8 implies that the error in the fractional cycle determination is minimized if $V_* = B$, meaning that the initial and final voltage measurements should take place as close as possible to the centerline of the intensity envelope, i.e., the DC level. Furthermore, the error is minimized if the A is large, i.e., the signal has high contrast. The small ΔA and ΔB also minimizes the error. The zone plate scheme is superior to the beamsplitter scheme in that ΔA can be small if the zone plate moves near to the centroid of the Gaussian intensity envelope, but it suffers from relatively low signal contrast.

3.1.2 Displacement measurement

The displacement sensor should measure the relative displacement of the stage to the phase-locked image. However, the image grating and the stage can move independently and randomly due to several factors such as vibrations, temperature, and so on. As will be shown later, in the homodyne experiment described here, a capacitance gauge with an accuracy of ± 16 nm is used without any environmental enclosure or a fringe-locking control system. In the SBIL, the displacement traveled by the stage is measured by heterodyne displacement measuring interferometers (DMIs) [20]. The static positioning error of the SBIL stage along the x axis is reported as around 30 nm [21], [22]. However, the stage error is corrected in real-time by a heterodyne fringe-locking system, which tries to minimize the image to stage motion.

3.1.3 Experiment

The homodyne experimental setup is depicted in Figure 3-6. An amplitude Fresnel zone plate is mounted on a translation stage that is driven by a New Focus Model 8302 picomotor. Figure 3-7 shows a scanning electron microscope (SEM) micrograph of the Fresnel zone plate. The zone plate has 200 zones, a minimum zone width of 207 nm, and a diameter of 127 μm. Due to the nondeterministic motion of the picomotor, the displacement traveled by the stage is measured using a capacitance gauge (ADETech., Model 4810) that has a linearity of ± 0.05 % [24]. Two coherent laser beams ($\lambda = 632.8$ nm) are incident on the Fresnel zone plate and diffracted to form moiré zone plates on the lens. The lens is positioned to sample the first order moiré zone plate and focus it onto a photodiode.

As the Fresnel zone plate is scanned, the optical power transmitted through the zone plate is measured at the photodiode. The analog-to-digital (A/D) conversion is handled by a National Instruments NI 6034E I/O board [25]. The capacitance gauge is also connected to the A/D board for the easier calculation of the image grating period. The experiment is carried out for incident angles of 20 degrees and 35 degrees using the same zone plate to demonstrate its capability in measuring different image grating periods.

3.1.4 Results and discussion

Thirty sets of period measurement were taken for each incident angle. Figure 3-8 shows signals sampled at the photodiode as the Fresnel zone plate was displaced for an incident angle of 20 degrees. The sample rate is at 5 kHz. A lot of noise is present primarily due to acoustics and excitations by the internal vibrations of the picomotor. For accurate detection of oscillations, the signals were filtered using an FIR low-pass filter (Kaiser Window) with a cutoff frequency of 10 Hz, a transition band of 15 Hz, and ≥ 60 dB attenuation in the stop band. The FIR filter was used to have a linear phase relationship between the raw and the filtered signals, and the Kaiser window is known to optimize the trade-off between main lobe sharpness and sidelobe amplitude

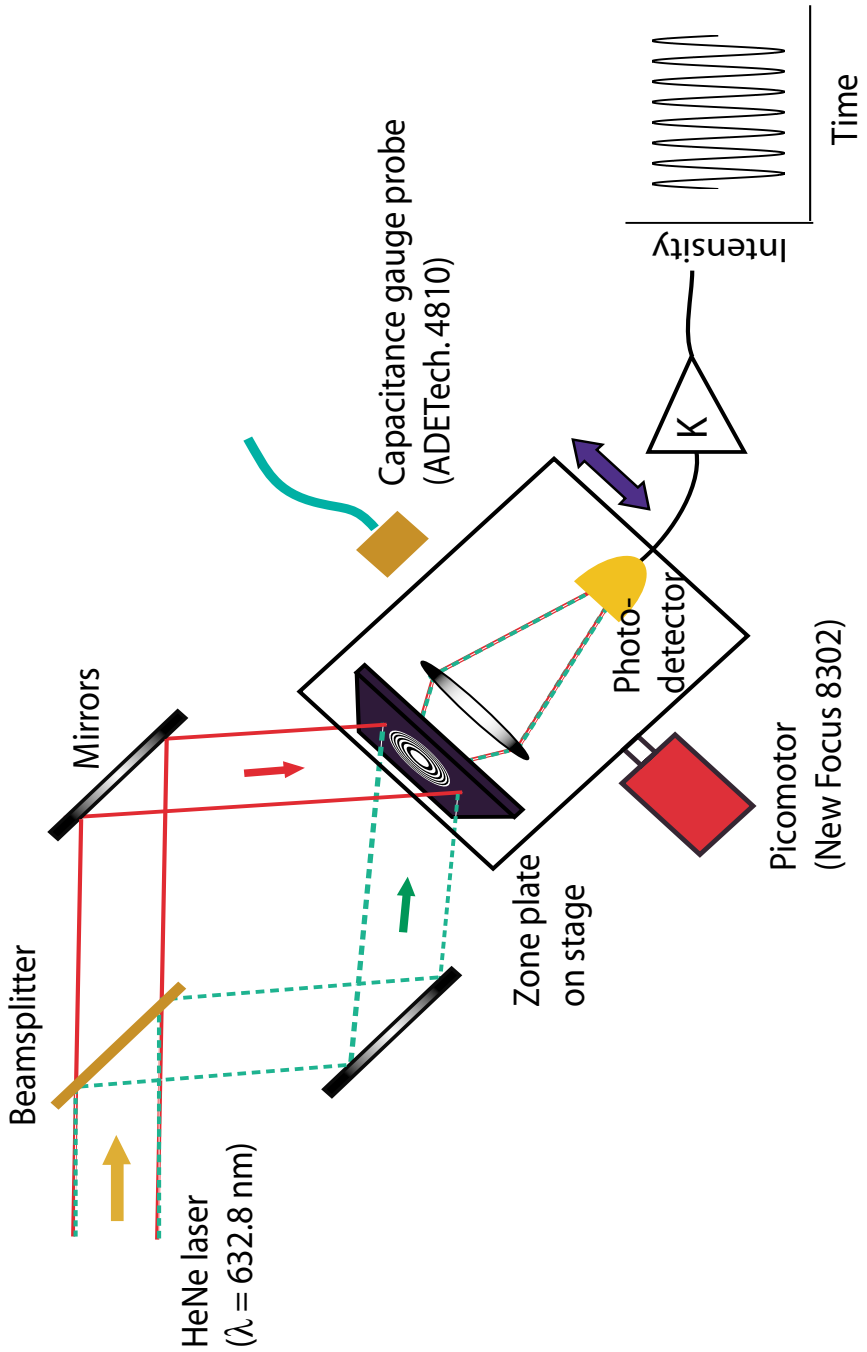

Figure 3-6: Schematics of the homodyne period measurement system. The photodiode measures the power fluctuations as the zone plate is scanned.

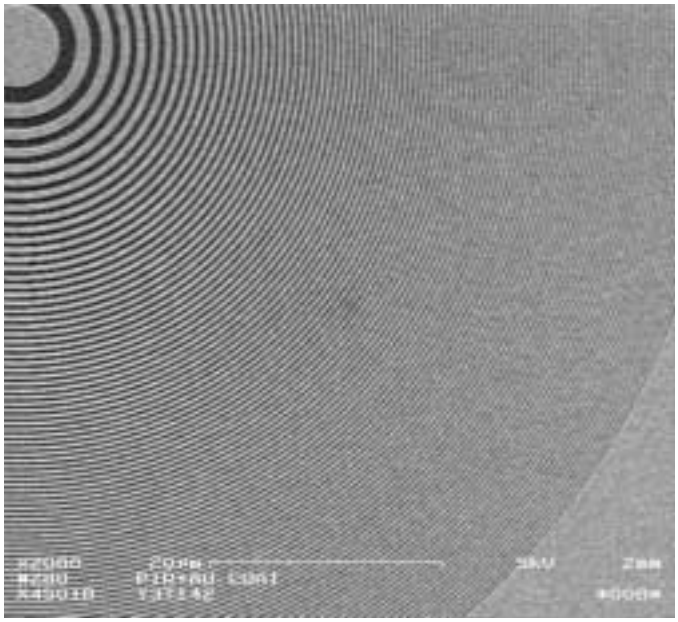

Figure 3-7: SEM micrograph of the amplitude Fresnel zone plate written by the LBNL *Nanowriter*. It has 200 zones, a minimum zone width of 207 nm, and a diameter of 127 μm.

[**?**]. The filtered signal is also shown in Fig. 3-8. With the knowledge of number of oscillations (N) and the distance traveled by the stage (D), the image grating periods were calculated.

For reference, a protractor with a resolution of 1 degree was used to measure incident angles. Based on the measured angle, the image grating periods are predicted by

$$\Lambda_p = \left(\frac{\lambda}{2\sin\theta}\right)_{\theta=\theta_i} \pm \left|\frac{\lambda}{2}\left(\frac{\cos\theta}{2\sin^2\theta}\right)_{\theta=\theta_i}\right| \Delta\theta, \tag{3.10}$$

where θ_i is the angle of incidence, and $\Delta\theta$ represents the angle measurement uncertainty due to the limited resolution of the protractor. Using Eqn. 3.10, the image grating period are predicted as 926$\pm$44 nm for an incident angle of 20 degrees and 552$\pm$14 nm for an incident angle of 35 degrees. From the period measurements, the mean image grating periods of 911.8 nm and 541.1 nm were obtained, respectively. The one-sigma repeatabilities were 1.1 nm and 0.9 nm for each case. The poor resolution of the angle measurement is a significant contributor to the discrepancy between the predicted and the measured periods.

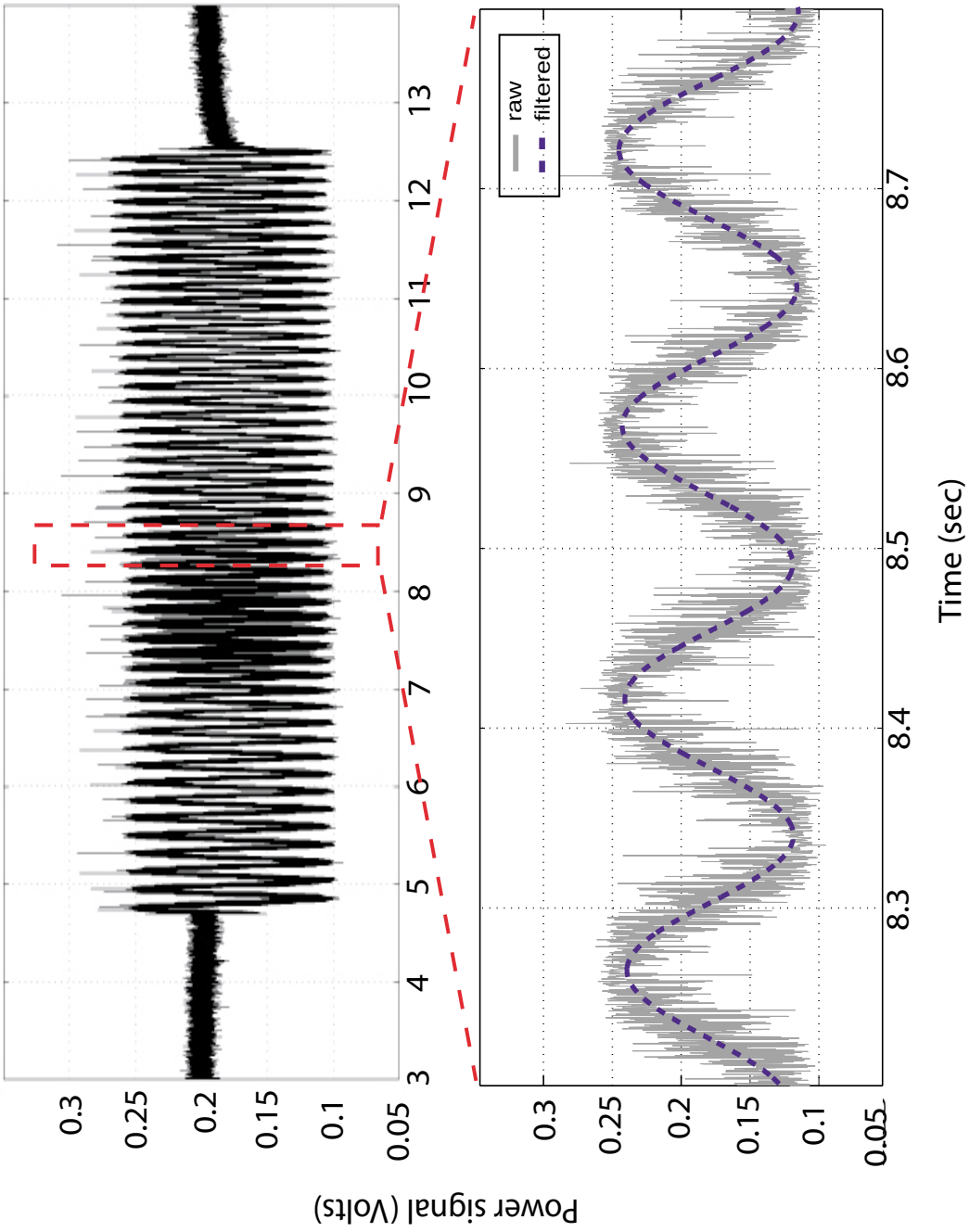

Figure 3-8: Raw and digitally filtered signals (sample rate = 5 kHz, angle of incidence = 20 degrees).

The period measurement uncertainty involves several factors. In our case, the period uncertainty is given by

$$\Delta\Lambda = \frac{1}{N_0}\Delta D - \frac{D_0}{N_0^2}\Delta N, \tag{3.11}$$

where N_0 and D_0 are the measured total number of oscillations and the distance traveled by the Fresnel zone plate, respectively. The ΔD and ΔN represent the uncertainties regarding their measurements. As for the uncertainty of the displacement measurement, the inaccuracy of the displacement sensor is dominant, compared to the absolute accuracy of the analog-to-digital converter (ADC), which is around 3 nm. Notice that the uncertainties are proportional to $1/N_0$ or $1/N_0^2$, so it can be reduced further by long travel of the translation stage, thereby increasing the number of oscillations (N_0).

Cosine errors in the alignment of the Fresnel zone plate, the displacement sensor, and the interferometric optics also result in bias errors. The Fresnel zone plate has been set to travel normal to the image grating lines within 0.5 mrad, which corresponds to an uncertainty of ± 0.6 nm and ± 0.2 nm for each case. The one-degree misalignment of the translation stage with the zone plate plane leads to an error of 0.015 % of the actual period.

Furthermore, the repeatability suffers from many error sources, including fringe drift due to the change of refractive index, vibrations, and acoustics. Note that the experiments have been performed without a properly designed low coefficient of thermal expansion (CTE) metrology frame, a fringe-locking system, or an environmental control.

3.2 Heterodyne period measurement

The interference of two coherent laser beams with different temporal frequencies produces an image grating with fringes that moves at their frequency difference. The heterodyne scheme measures the phase of the image grating, and obtains its spatial period by using the relation

$$f_x = \frac{1}{\Lambda} = \frac{1}{2\pi}\frac{\partial\phi}{\partial x}, \tag{3.12}$$

where f_x is the spatial frequency along the x axis, and ϕ is the spatial phase. Compared to the homodyne case, the heterodyne detection offers better signal-to-noise ratio, reduced sensitivity to differential amplitude variations, and less drift due to $1/f$ noise [28], [29]. Indeed, the optical power transmitted through the phase zone plate installed in the SBIL is too low to use the homodyne scheme. However, the heterodyne scheme allows measuring the spatial period of the image grating.

3.2.1 Principle of operation

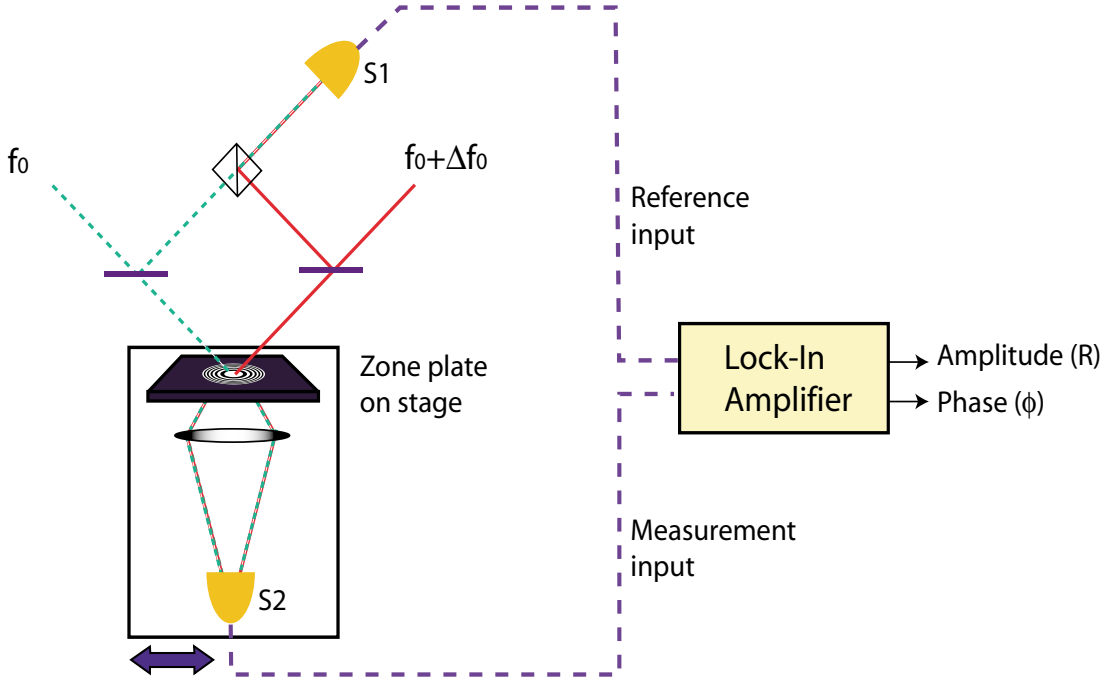

Figure 3-9: Heterodyne period measurement concept. The interference of two heterodyne beams generates a reference signal to the lock-in amplifier, and its frequency shift caused by the zone plate scan is sampled and compared to the reference signal of the lock-in amplifier.

Figure 3-9 shows the concept of heterodyne detection of image grating period. Two beams with a frequency difference of Δf_0 are overlapped at the beamsplitter interface, and propagate onto the detector (S1), which is connected to the external

reference input of the lock-in amplifier. Then, the S1 measures the interference signal between two beams, and its phase is given by

$$\phi_1 = 2\pi\Delta f_0 t + \Delta\phi, \tag{3.13}$$

where $\Delta\phi$ represents the constant phase difference of the left and right beam. The interference of two beams on the Fresnel zone plate produces an image grating moving at their frequency difference, Δf_0. However, as the stage moves across the image grating, the frequency shift is sampled at the detector (S2), and it is described by

$$\phi_2 = 2\pi\Delta f_0 t \pm \frac{2\pi}{\Lambda} v t + \Delta\phi = \left(2\pi\Delta f_0 \pm \frac{2\pi}{\Lambda} v\right) t + \Delta\phi, \tag{3.14}$$

where v stands for the stage velocity, and the operator $\pm$ accounts the direction of the stage relative to the moving image grating. The signal S2 is connected to the measurement input of the lock-in amplifier.

The lock-in amplifier uses a phase-locked-loop (PLL) and the external reference input to generate the reference signal. The PLL in the lock-in amplifier locks the internal reference oscillator to this external reference, resulting in reference sine and cosine waves at Δf_0 with a fixed phase shift of ϕ_r. Since the PLL actively tracks the external reference, changes in the external reference frequency do not affect the measurement.

The measurement signal is amplified and multiplied by the lock-in reference signals using phase-sensitive detectors (PSDs). Assume that the measurement signal is represented as

$$V_{sig} = V_m \sin\left[\left(2\pi\Delta f_0 \pm \frac{2\pi}{\Lambda} v\right) t + \Delta\phi\right], \tag{3.15}$$

where V_m is the input signal amplitude. Then, the ouput of the PSD is simply the product of reference signal and measurement signal. For one PSD,

$$V_1 \;=\; V_m V_r \sin\left[\left(2\pi\Delta f_0 \pm \frac{2\pi}{\Lambda} v\right) t + \Delta\phi\right] \sin\left[2\pi\Delta f_0 t + \phi_r\right]$$

$$= \frac{1}{2}V_m V_r \cos\left[\pm\frac{2\pi}{\Lambda}vt + \Delta\phi - \phi_r\right] - \frac{1}{2}V_m V_r \cos\left[\left(4\pi\Delta f_0 \pm \frac{2\pi}{\Lambda}v\right)t + \phi_r + \Delta\phi\right], \tag{3.16}$$

and, for the other PSD,

$$\begin{aligned} V_2 &= V_m V_r \sin\left[\left(2\pi\Delta f_0 \pm \frac{2\pi}{\Lambda}v\right)t + \Delta\phi\right]\cos\left[2\pi\Delta f_0 t + \phi_r\right] \\ &= \frac{1}{2}V_m V_r \sin\left[\pm\frac{2\pi}{\Lambda}vt + \Delta\phi - \phi_r\right] + \frac{1}{2}V_m V_r \sin\left[\left(4\pi\Delta f_0 \pm \frac{2\pi}{\Lambda}v\right)t + \Delta\phi + \phi_r\right]. \end{aligned} \tag{3.17}$$

If those PSD outputs are passed through a low-pass filter, the high frequency AC signals are removed. Then, the filtered signals are

$$X = \frac{1}{2}V_m V_r \cos\left[\pm\frac{2\pi}{\Lambda}vt + \Delta\phi - \phi_r\right], \tag{3.18}$$

$$Y = \frac{1}{2}V_m V_r \sin\left[\pm\frac{2\pi}{\Lambda}vt + \Delta\phi - \phi_r\right], \tag{3.19}$$

assuming $\Delta f_0 \gg v/\Lambda$. Now we have two outputs, and these two quantities represent the signal as a vector relative to the lock-in reference oscillator. X is called the "in-phase" component and Y the "quadrature" component. By computing the magnitude (R) of the signal vector, the phase dependency is removed.

$$R = \sqrt{X^2 + Y^2} = V_m V_r/\sqrt{2}. \tag{3.20}$$

Here, R measures the signal amplitude and does not depend on the phase between the signal and lock-in reference. The phase of the signal vector is also calculated by

$$\varphi = \arctan\left(\frac{Y}{X}\right) = \pm\frac{2\pi}{\Lambda}vt + \Delta\phi - \phi_r = \pm\frac{2\pi}{\Lambda}\varepsilon + \Delta\phi - \phi_r. \tag{3.21}$$

Note that the image grating period can be obtained directly by taking derivative of the phase output of the lock-in amplifier with respect to the time or the displacement,

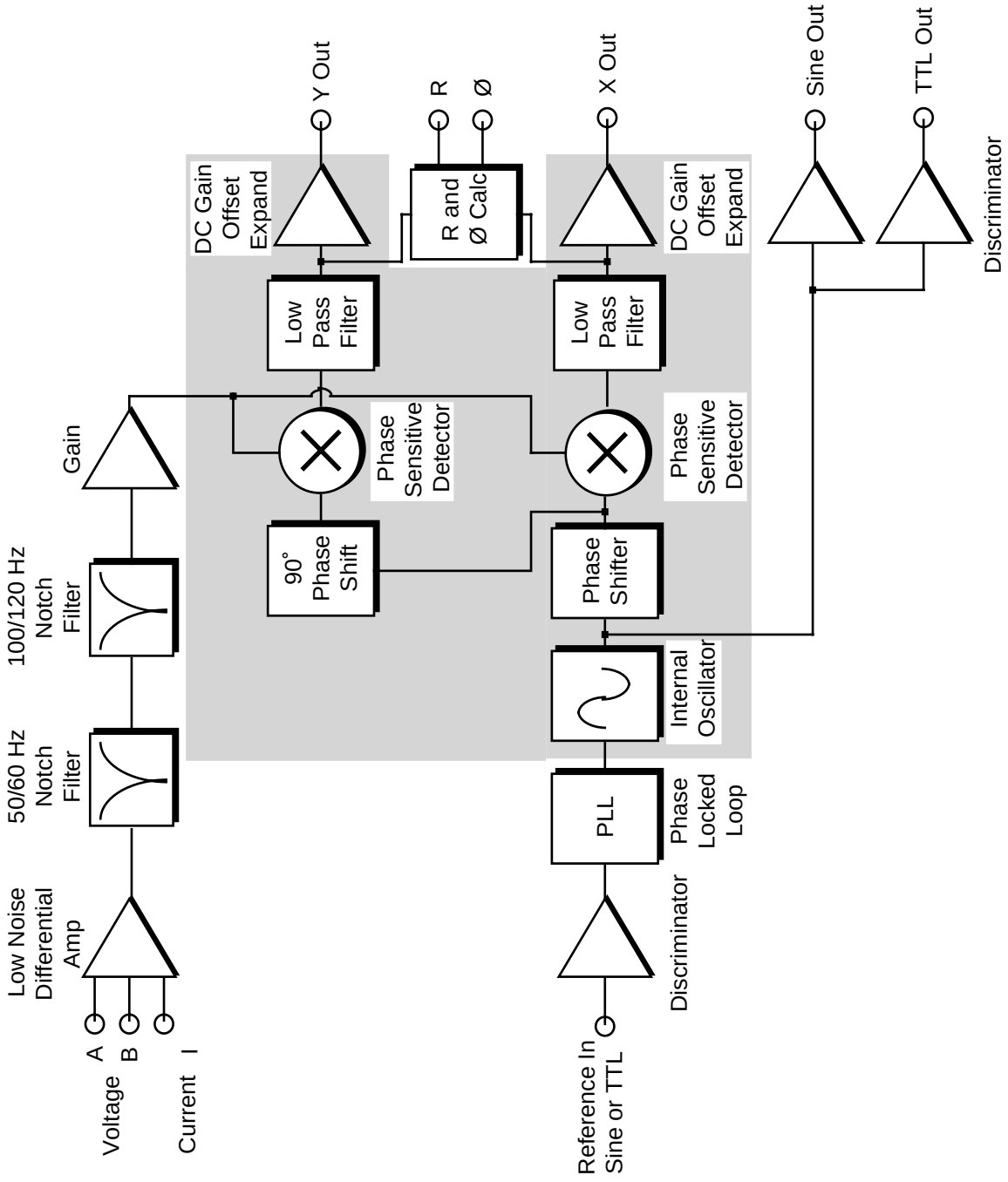

Figure 3-10: Functional block diagram of the lock-in amplifier, Stanford Research Systems, SR830.

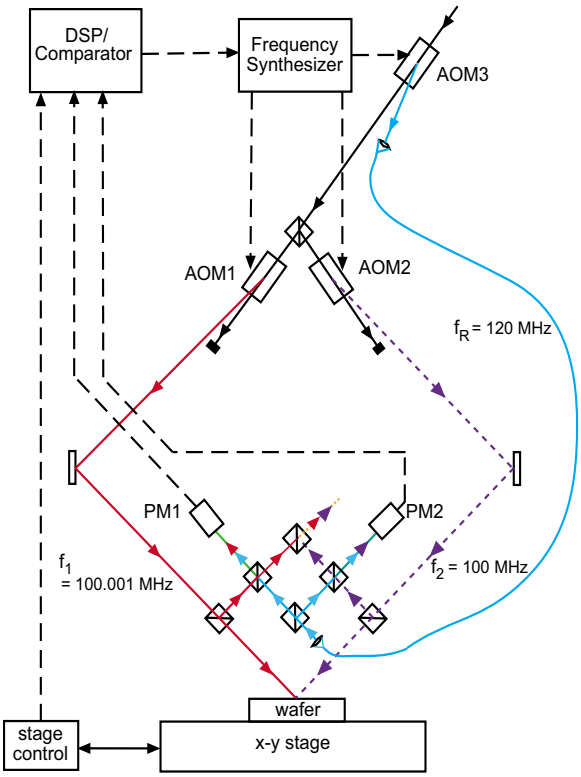

Figure 3-11: SBIL writing mode for two heterodyne beams. By setting the frequencies to the acousto-optic modulators (AOMs) and combining the appropriate diffracted beams, one generates two heterodyne signals at phase meters (PM) 1 and 2. A digital signal processor (DSP) then compares the signals and drives AOM1 to control the phase difference between the two arms to increase linearly.

which is denoted by ε. For reference, the functional block diagram of the lock-in amplifier (Stanford Research Systems, SR830), which is used in the experiment, is shown in Fig. 3-10 [30].

3.2.2 Heterodyne fringe controller

As in the homodyne case, the image grating produced by interference of two heterodyne beams should be locked to move at the frequency difference relative to the stage.

Figure 3-11 shows a schematic of the SBIL writing mode, which is modified for the heterodyne period measurement. A laser beam ($\lambda = 351.1$ nm, $f_0 \approx 854$ THz) is incident onto the acousto-optic modulator AOM3, which splits off a weak first-order reference beam with frequency $f_R = f_0 + 120$ MHz. The undiffracted zeroth-order

beam is then split by a grating beam splitter. Each of two first-order beams then propagates through another AOM (AOM1 and AOM2). The AOM1 is set to generate a strong first-order diffracted beam at $f_1 = f_0 + 100.001$ MHz, while the AOM2 is configured to generate a first-order beam at $f_2 = f_0 + 100$ MHz. The zeroth orders are dumped. Both arms are reflected by mirrors to intersect at angle 2θ on the zone plate mounted stage, generating an image grating with period $\Lambda = \lambda/2\sin\theta$. Close to the wafer, each beam is sampled by a weak pickoff splitter. Each beam is then combined with one-half of the reference beam (f_R). Thus two heterodyne signals of 20 MHz and 20.001 MHz are generated, which is then guided through fibers to their corresponding phase meters, PM1 and PM2. The phase readings ϕ_1 and ϕ_2 from PM1 and PM2, respectively, are compared by a digital signal processor, which then calculates the change in the driving frequency of AOM1 that is necessary to lock the interference fringe relative to the stage.

Paul Konkola has implemented the heterodyne fringe locking controller, and demostrated its short-term stability as one hundredth of a period. However, since it has been implemented based on the typical SBIL writing mode ($f_1 = f_2 = f_0 + 100$ MHz), the fringe locking control algorithm should be modified. Reference [22] details the stage control algorithm, in which the fringe locking error is described by

$$\phi_{fle} = \phi_1 - \phi_2 - [\phi_{xe}\cos\alpha + \phi_{ye}\sin\alpha]\,. \tag{3.22}$$

Here, ϕ_1 and ϕ_2 are the phase readings from PM1 and PM2, respectively, and α refers to the angle between grating direction and the scan direction. Thus, if the stage moves perfectly perpendicular to the grating lines, $\alpha = 0$. The ϕ_{xe} and ϕ_{ye} are the phase errors along the x and the y axes, and they are given by

$$\phi_{xe} = \phi_{xref} - \phi_x + (K_1\phi_x + K_2)\,\phi_{refrac}, \tag{3.23}$$

$$\phi_{ye} = \phi_{yref} - \phi_y. \tag{3.24}$$

The ϕ_{xref} and ϕ_{yref} stand for the reference phase counts along the x and y axes, and

ϕ_x and ϕ_y are the phase readings from the XY stage interferometers. The ϕ_{refrac} is the phase reading from the x axis refractometer that is installed to compensate the wavelength variation, and the constants K_1 and K_2 are the refractometer coefficients found by Paul Konkola empirically [22]. In the current algorithm, the controller tries to minimize the error toward zero.

For our heterodyne measurement, the difference between two phase readings, ($\phi_1 - \phi_2$), increases linearly with the clock count, since there is a frequency difference of 1 kHz. In order to conduct fringe locking for heterodyne cases, the algorithm should modified as

$$\phi_{fle} = \phi_m - \phi_2 - [\phi_{xe} \cos\alpha + \phi_{ye} \sin\alpha] , \tag{3.25}$$

where

$$\phi_m = \phi_1 - \phi_1(0) - C_f T. \tag{3.26}$$

Here, $\phi_1(0)$ is the phase reading from PM1 at T=0, C_f is the slope determined by the frequency difference of heterodyne beams, and T the clock count. So, the slope has a unit as [phase counts / clock counts].

3.2.3 Experiment

Figure 3-12 shows a photograph of the heterodyne experimental setup in the Nanoruler. A phase zone plate is mounted to the stage along with the lens and the photodiode. The zone plate has 350 zones, a minimum zone width of 194 nm, and a diameter of 193 μm. The zone plate is aligned such that its plane is identical to the substrate plane within 0.5 μm. The alignment is conducted by using a displacement sensor (Federal Precision Height Stand, Model 2400) and tilt screws of the zone plate mount. Firstly, the probe tip of the sensor is placed on the substrate, and then its zero point is set to the current position, i.e., the substrate plane in order for the following measurements to be referenced to the point. After that, the stage moves to place the probe tip on the zone plate. Scanning the stage, the zone plate is aligned

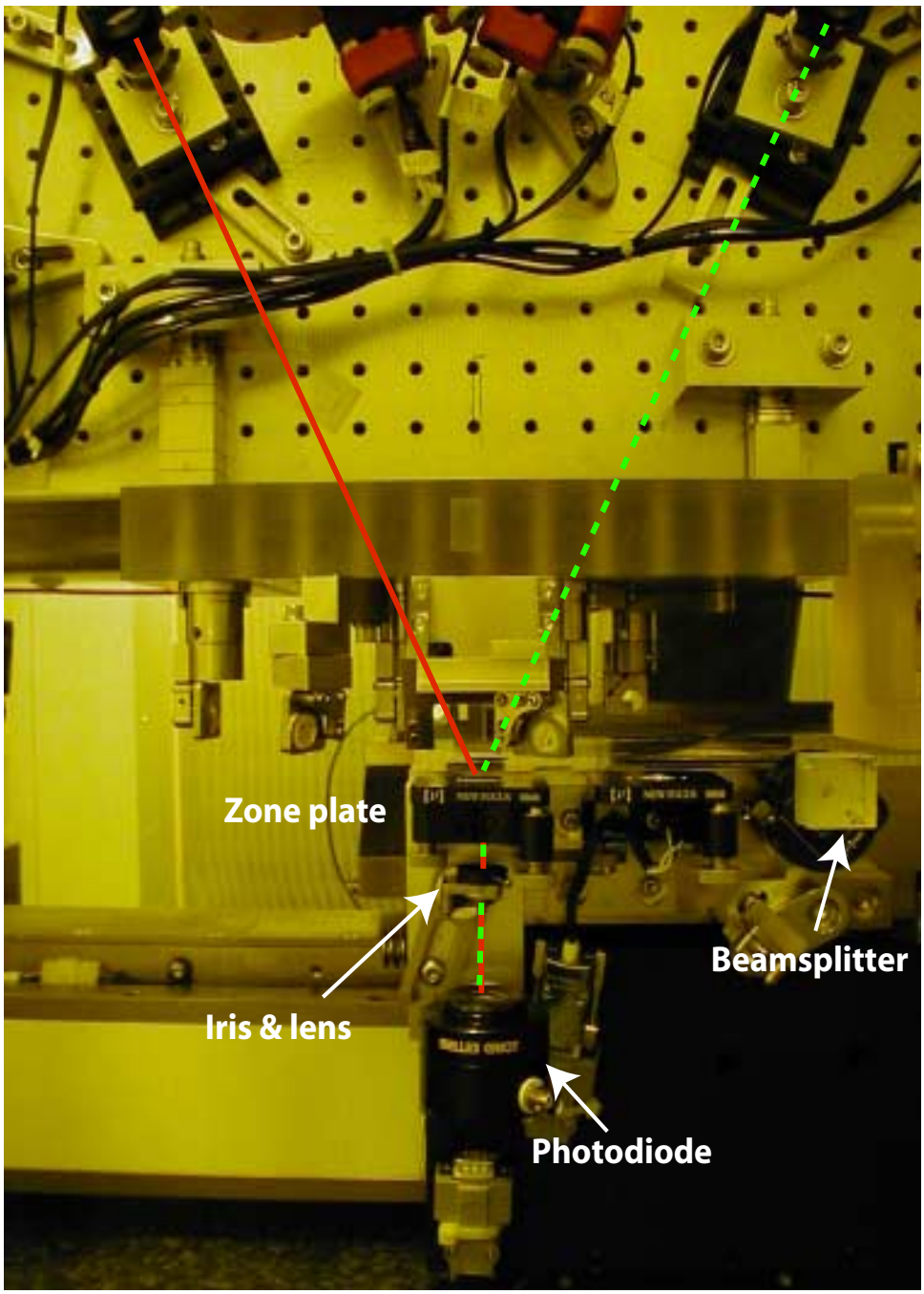

Figure 3-12: The heterodyne period measurement setup

by the efforts to minimize the deviation of its readout from the zero point.

The beam alignment system is used to overlap the left and right arms in position, and to equalize two angles of incidence. For the experiment, the beam alignment software has been operated in the beamplitter mode [19]. After the beam alignment is completed, the stage moves to the position such that two beams are incident on the zone plate. Then, the heterodyne beams are generated by changing the driving frequency of the AOMs. The frequencies of AOM1 is set to 100.001 MHz, for AOM2, 100 MHz, and for AOM3, 120 MHz. Thus, an image grating with fringes that move at 1 kHz is produced. The lens under the zone plate images the first-order moiré zone plate and focuses it onto the photodiode, which is connected to the measurement input of the lock-in amplifier (SR830). In order to detect the reference signal, a high-frequency photodiode (Melles-Griot, 13 DAH 005) is set up under the optical bench.

3.2.4 Results and discussion

The period measurement has been conducted without a properly implemented fringe locking controller because of its unavailability on July, 2003. I used 100 msec as a time constant of the low-pass filter in the lock-in amplifer, since it takes time to filter the outputs of the PSDs. The stage moved by twenty steps, and the step size is 40 nm. Since the current Nanoruler is set up to produce a grating of nominal period 400 nm, one can expect two cycles in the amplitude and phase outputs of the lock-in amplifier. Indeed, it is the case.

Figure 3-13 shows the outputs of the lock-in amplifier. After each step, the data over 10 seconds were taken, and their average value was recorded in order to minimize the effect of the phase jitter. Since the phase output range of the lock-in amplifer is -180$\sim$180 degrees, the jump from 180 degrees to -180 degrees is observed. For the easier calculation of image grating period, the phase measurement data is unwrapped by using MATLAB, and the unwrapped one is shown in Fig. 3-14. It demonstrates linear phase progression by the displacement of the stage. Based on the result, the image period is obtained as

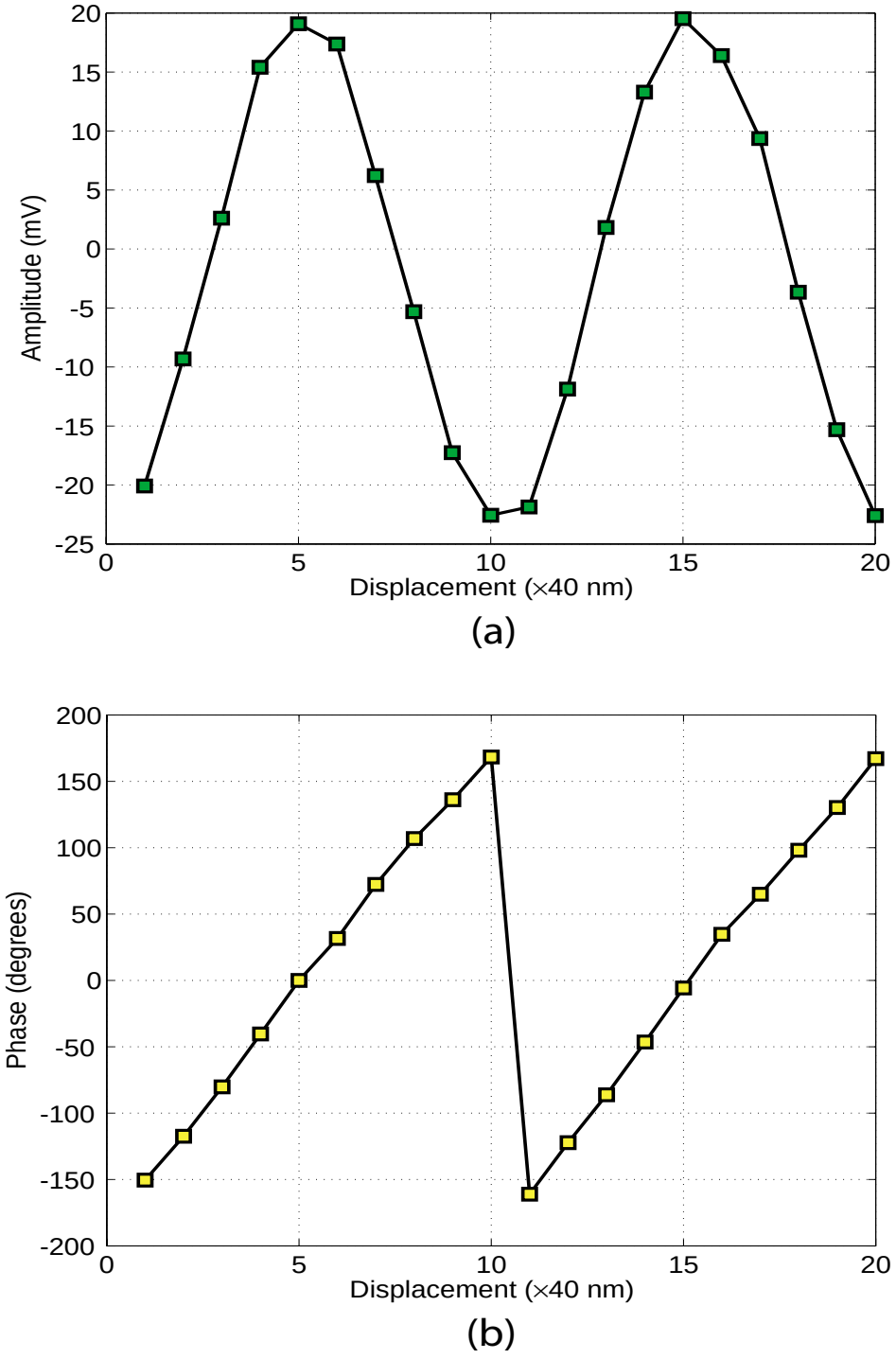

Figure 3-13: The heterodyne period measurement. (a) Amplitude variation by the stage displacement. (b) Phase variation by the stage displacement.

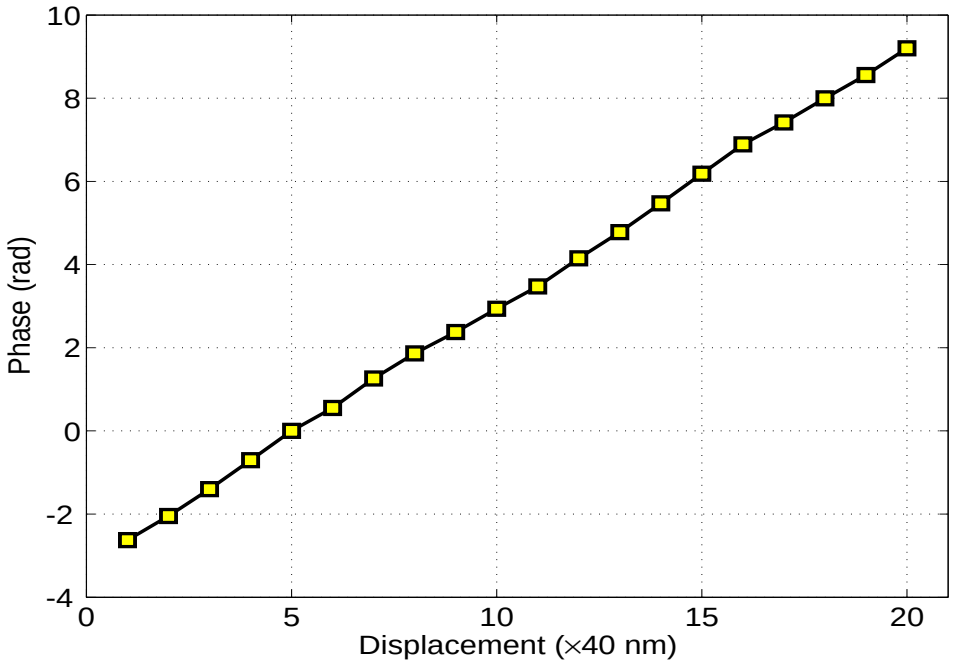

Figure 3-14: Unwrapped phase data

$$\Lambda = \left[\frac{1}{2\pi}\frac{\Delta\phi}{\Delta x}\right]^{-1} = \left[\frac{1}{2\pi}\cdot\frac{9.199-(-2.626)}{40\cdot(20-1)}\right]^{-1} = 403.789 \text{ nm}. \tag{3.27}$$

As a reference, the period measured by the rectangular beamsplitter is 401.246 nm [19]. The relatively stable phase progression shown in Figure 3-14 is primarily due to the much more stabilized environment in the Nanoruler.

3.3 Contrast fluctuation measurement

In order to demonstrate contrast variation of optical power by varying image grating periods, a simple interferometry has been designed and implemented.

3.3.1 Experiment

Figure 3-15 shows the experimental setup, basically similar to that of the homodyne period measurement. The difference is that two mirrors in both arms are mounted on translation stages, which are driven by micrometers. Thus, once a measurement is completed for an image grating period, the subsequent measurements can be per-

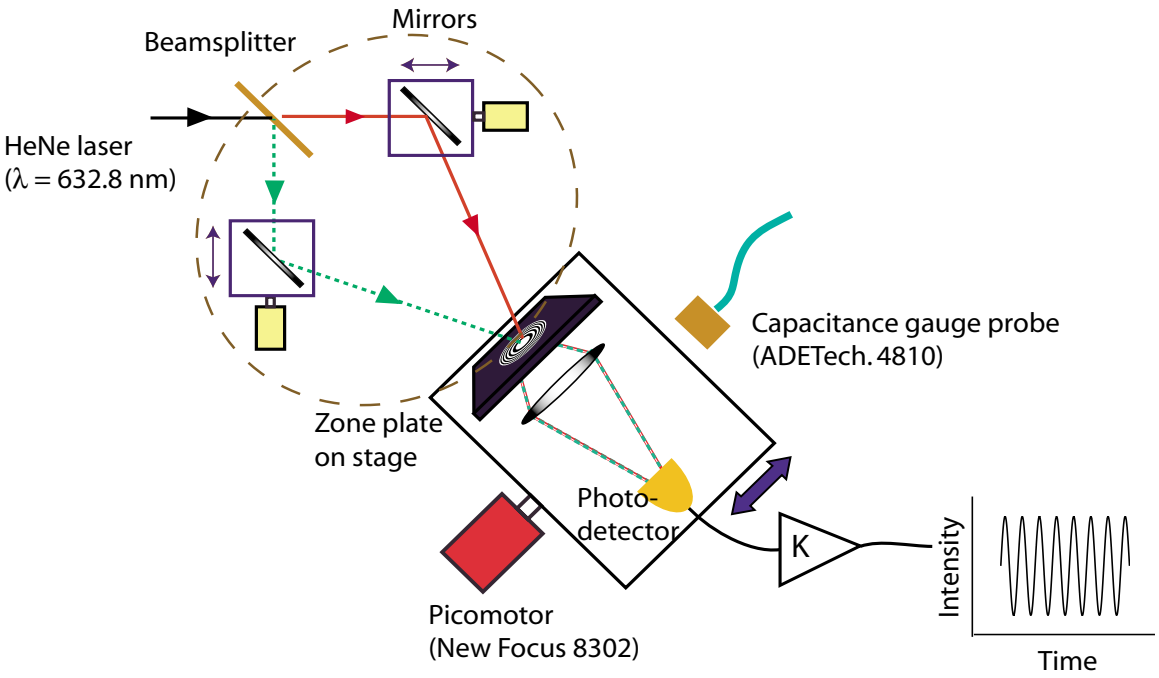

Figure 3-15: Contrast variation measurement system. It is similar to the homodyne period measurement system except that two mirrors are mounted to the translation stage to vary incident angles.

formed by translating the mirrors by the same distance, and adjusting the mirrors such that the beams are incident on the zone plate. In the setup, the mirrors are set to translate normal to the beam propagation direction.

The HeNe laser ($\lambda = 632.8$ nm) and a phase zone plate with 100 zones, a diameter of 322 μm, and an innermost zone radius of 16 μm are used. The micrometer (New-Focus, Model 9353) has a resolution of 10 μm, which is the step size of the mirror translation. As before, the data acquisition is handled by the National Instruments A/D board.

Once the optical power is measured for an incident angle as the zone plate moves, the signal is filtered using an FIR filter (Kaiser Window) to compute the contrast of optical power. The filter specifications should be modified depending on the image grating period. The contrast is evaluated by

$$C = \frac{P_{max} - P_{min}}{P_{max} + P_{min}} \tag{3.28}$$

where P_{max} and P_{min} are the averaged peak and valley values observed at the sinu-

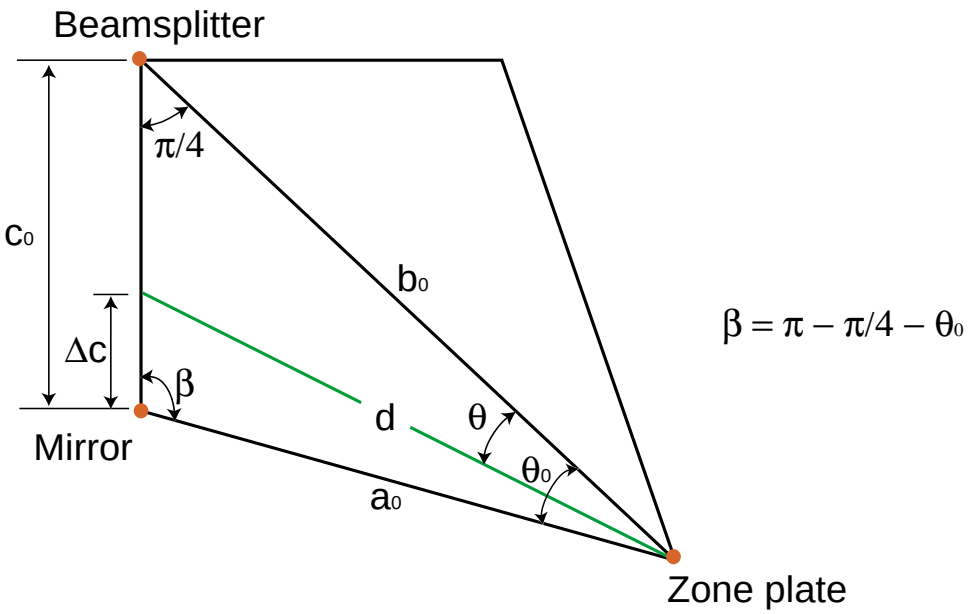

Figure 3-16: Geometry for incident angle calculation.

soidal optical power variations. Using the initial setup parameters and the mirror translation step size, the image grating period of each measurement can be derived. The portion indicated with the dashed lines in Fig. 3-15 is redrawn in Fig. 3-16. The a_0, b_0, and c_0 are the initial lengths from the mirror to the zone plate, from the beamsplitter to the zone plate, and from the beamsplitter to the mirror, respectively. Also, θ_0 is the initial incident angle and θ is the incident angle after the mirror is displaced towards the zone plate by Δc. The length from the beamsplitter to the mirror represented by $(c_0 - \Delta c)$ can be expressed by using the second cosine law:

$$(c_0 - \Delta c)^2 = b_0^2 + d^2 - 2b_0 d\cos\theta, \tag{3.29}$$

where d stands for the length from the mirror to the zone plate and θ is the incident angle after the mirror is displaced. A closer examination of the geometry reveals that d can be also obtained using

$$d^2 = (\Delta c)^2 + a_0^2 - 2a_0(\Delta c)\cos\beta = (\Delta c)^2 + a_0^2 - 2a_0(\Delta c)\cos\left(\pi - \pi/4 - \theta_0\right). \tag{3.30}$$

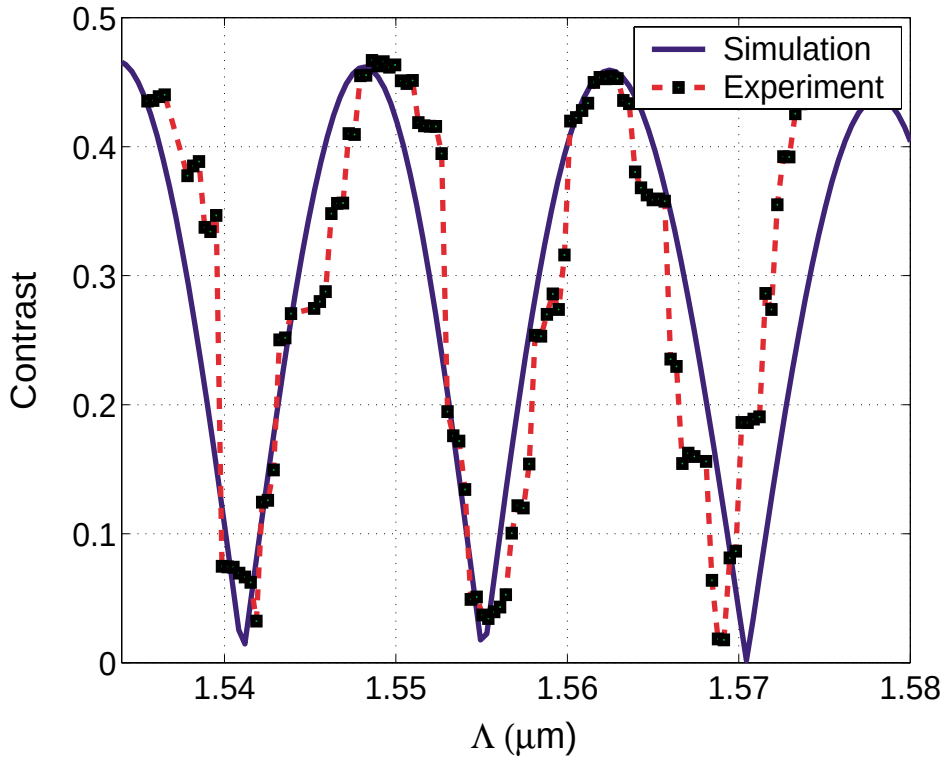

Figure 3-17: Contrast measurement results.

Therefore, the incident angle θ can be obtained using Eqns. (3.29) and (3.30) together, so that image grating periods are predicted.

3.3.2 Results and discussion

The initial interferometry is set up to an incident angle of 11.6 degrees. After the initial measurement, it was followed by sixty measurements by translating the mirrors, or consequently varying incident angles. Figure 3-17 shows the experimental results along with the simulation result. Surprisingly, the experimental results shows high correspondence to the simulation results, even though there are many uncertainties in terms of the incident angle measurement and the alignment. In any case, it provides a confirmation that the contrast of optical power varies with image grating period for a given Fresnel zone plate.

Chapter 4

Conclusions

The work presented in this thesis is on the research into a novel image metrology using a special diffractive structure. The role of image metrology in scanning-beam interference lithography (SBIL) is critical, since it ensures the precise stitching of subsequent scans. The current SBIL is configured to produce gratings of nominal period 400 nm. However, it is expected to be capable of patterning general gratings such as linear or chirped gratings by varying beam incident angles or rotating the beams during the operation. In this case, image grating metrology should be applicable to measure a wide range of grating periods regardless of changes in grating orientation.

In that aspect, a Fresnel zone plate is a natural choice because of its unique properties. Its axial symmetry allows us to measure image periods, immune to changes in grating orientations. Its chirp feature is also important because it can measure a wide range of grating periods.

In order to understand the basic principle of the Fresnel zone plate and the physics of image metrology, extensive theoretical studies have been made. Based on the understanding of the Fresnel zone plate, it has been found that the zone plate can be regarded as the superposition of one plane wave and multiple converging and diverging spherical waves with different focal lengths. Indeed, it provides an intuitive and interesting way to understand the formation of the moiré zones. Moreover, it helps to define the range of image periods measurable for a given zone plate. The moiré zone plates are produced by the interference of diffracted waves by a zone plate,

and they have also been found in a closed mathematical form. Using the irradiance of the moiré zone plates, the image period can be derived. The contrast (or visibility) of optical power with varying image periods was also investigated. The question is whether one can use the same zone plate to characterize a range of image grating periods. Remarkably, it was found that it is a chirped sinusoidal function of image period. Namely, the contrast could be zero for some image periods, where the image metrology cannot be used.

Experiments have been designed and performed to verify the findings in the theoretical work. Homodyne period measurement has been performed for two image periods using the same amplitude zone plate. The zone plate was successful in measuring the image periods with nanometer-level repeatability. As for the heterodyne period measurement, a phase zone plate was installed to the current SBIL prototype system, the Nanoruler. Using the phase changes of the optical power transmitted through the zone plate as the stage is displaced, the image period was calculated and compared with the result of the beamsplitter scheme, which is currently used in the Nanoruler. Even without a properly designed fringe locking controller, it follows the period measured by the beamsplitter closely. The contrast variation measurement was also carried out with the same experimental setup of the homodyne case. In the experiment, a phase zone plate was used. For a range of image periods, contrast varies as a chirped function similar to the zone plate. As the image period is decreased, the contrast varies more frequently.

With two conditions for image metrology to satisfy: immune to grating orientations and capability of measuring a wide range of periods, the use of a Fresnel zone plate would be an excellent choice. Indeed, it can be used to characterize image gratings as long as its period is in the range of high contrast for a given zone plate. However, the zone plate scheme is, strictly, limited by its low optical power throughput, since the optical power of the interference of multiple spherical waves is used in the measurement.

Future work may include a study of how to increase optical power for image grating metrology using a Fresnel zone plate. Also, the effect of the amplitude variation of the

incident waves on the phase measurement and the phase measurement error through optical power detection are the critical aspects to be fully understood.

Appendix A

Power estimation of moiré zone plates

The optical power of moiré zone plates must be higher than the noise equivalent power (NEP) of a sensor to detect power fluctuations as the Fresnel zone plate moves. The innermost zone of the first-order moiré zone plate is used for the measurement, so its power estimation at the design stage would help the implementation of the image grating metrology using a Fresnel zone plate.

Consider again a diffraction of two plane waves by a Fresnel zone plate as shown in Figure A-1. Two plane waves are assumed to have a wavelength of λ and an incident angle of θ. The optical power of an incident plane wave is P_0. As they are diffracted by the Fresnel zone plate, the diffracted waves are superimposed in the observation plane (x', y'), forming two diffraction zone plates. The moiré zone plates are produced by the interference of these two diffraction zone plates. The image grating generated by the interference of two plane waves has a diameter of d_0, and the Fresnel zone plate is characterized by the innermost zone radius ρ and diameter d_f. The power of each diffraction zone plate can then be approximated as

$$P_c = 2\eta \left(\frac{d_f}{d_0}\right)^2 P_0. \tag{A.1}$$

Here, I considered only the $\pm$1st diffraction orders which have the highest power,

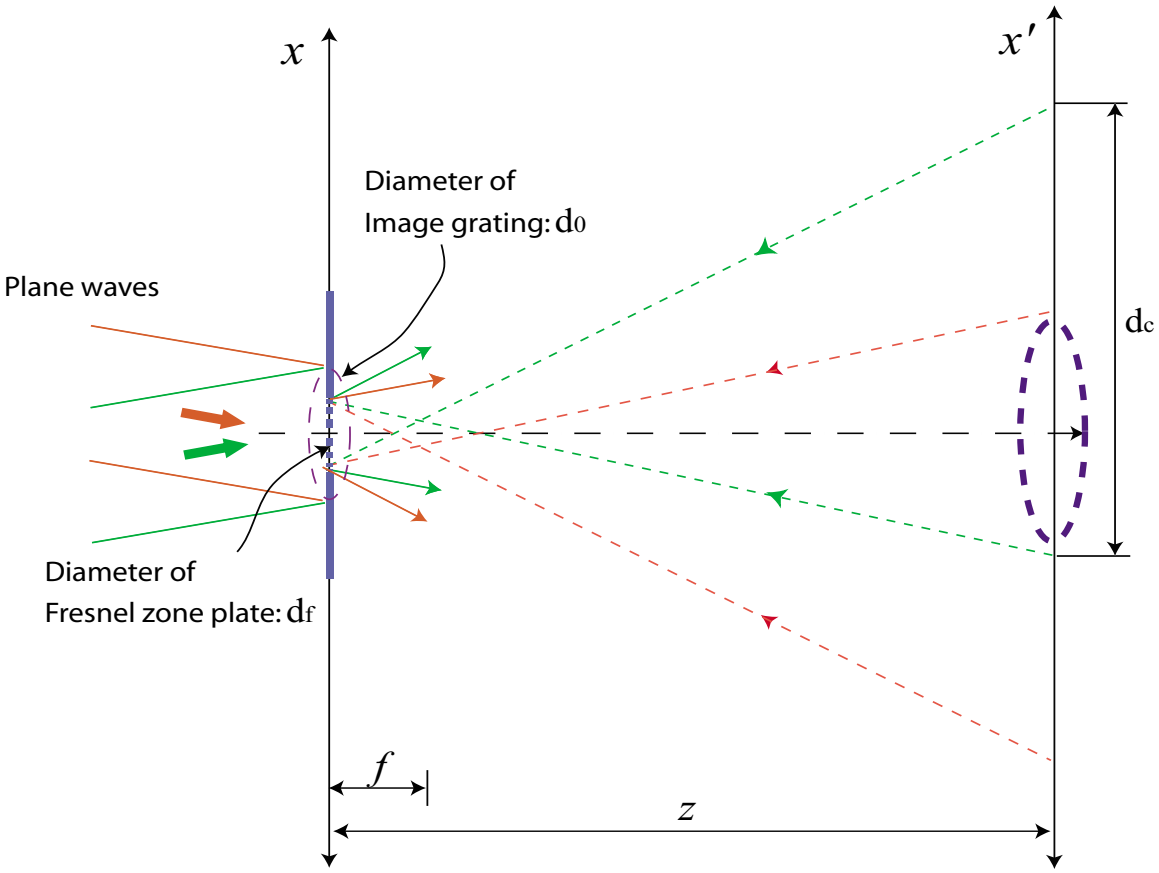

Figure A-1: Diffraction of two plane waves by a Fresnel zone plate.

and the η represents the first-order diffraction efficiency. Namely, the power of a diffraction zone plate is approximately equal to the sum of the power of the $\pm$1st order diffraction waves, which are reduced by the area ratio of the Fresnel zone plate to the image grating, beforehand.

Figure A-2 illustrates two overlapped circles. Two circles represent the diffraction zone plates and the overlap region is the interference region of the diffraction zone plates in the observation plane. The moiré zone plates are produced in the interference region. As illustrated, the area of overlap may be regarded as being equal to four times the shaded area B of the circular sector $A + B$. The diameter of the circle can be found by using the geometry in Figure A-1. Since $f \ll z$, the diameter of the circle, d_c, is given by

$$d_c = \frac{z}{f} d_f, \tag{A.2}$$

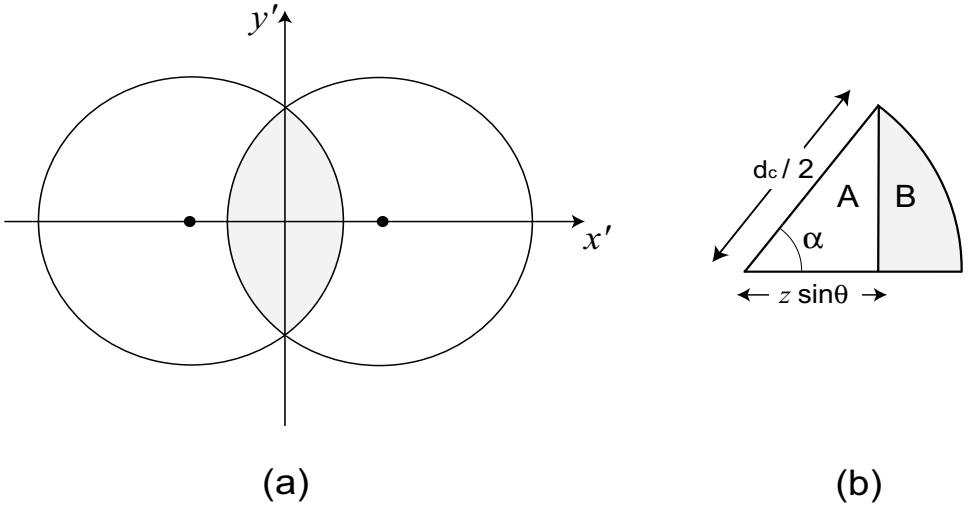

Figure A-2: Calculation of the area of overlap of two displaced circles. (a) Overlapping circles, (b) geometry of the calculation.

where the f is the primary focal length of the Fresnel zone plate, and z is the free-space propagation distance. The focal length f is related to the innermost zone radius ρ of the Fresnel zone plate by [??]

$$f = \frac{\rho^2}{\lambda}. \tag{A.3}$$

The center of circle is separated by $z \sin\theta$ from the origin, assuming that θ is small. Thus, the area of the circular sector is

$$\text{Area}(A+B) = \left[\frac{\alpha}{2\pi}\right]\left(\pi\frac{d_c^2}{4}\right) = \left[\frac{\arccos(2f\sin\theta/d_0)}{2\pi}\right]\left(\pi\frac{d_c^2}{4}\right) \tag{A.4}$$

while the area of the triangle A is

$$\text{Area}(A) = \frac{1}{2}(z\sin\theta)\sqrt{\frac{d_c^2}{4} - (z\sin\theta)^2}. \tag{A.5}$$

Finally, the power of the interference region can be evaluated by

$$P_b = 2r_1 P_c, \tag{A.6}$$

where r_1 is the area ratio defined by

$$r_1 = \frac{4[\text{Area}(A+B) - \text{Area}(A)]}{\pi(d_c^2/4)} = \frac{4[\text{Area}(A+B) - \text{Area}(A)]}{A_c} \tag{A.7}$$

or

$$r_1 = \begin{cases} \frac{2}{\pi}\left[\arccos(\gamma) - \gamma\sqrt{1-\gamma^2}\right] & \gamma \leq 1 \\ 0 & \text{otherwise} \end{cases} \tag{A.8}$$

The quantity γ is defined by

$$\gamma = \frac{\sin\theta}{d_0/2f} = \frac{\sin\theta}{N.A.}. \tag{A.9}$$

It says the same argument discussed earlier in that the incident angle of the plane wave should be smaller than N.A. of the Fresnel zone plate for the diffraction zone plates to be superimposed on each other in the observation plane. Since the innermost zone of the first-order moiré zone plate is sampled to maximize the contrast, the area of the innermost zone needs to be calculated. The radius of the innermost zone can be found by examining Eqn. (2.37). Using the paraxial approximation, the innermost zone radius is

$$\rho_z = \frac{\lambda z}{\rho}. \tag{A.10}$$

In order to obtain the power of the innermost zone of the first order moiré zone plate, Eqn. (A.6) needs to be multiplied by another area ratio defined by

$$r_2 = \frac{\pi\rho_z^2}{A_c}, \tag{A.11}$$

so its power is evaluated by

$$P_z = 2r_1 r_2 P_c = 4r_1 r_2 \eta \left(\frac{d}{d_0}\right)^2 P_0. \tag{A.12}$$

The P_z must be higher than the NEP of a sensor to measure power fluctuations of the moiré zone plate. Figure A-3 shows an example of the calculation of the innermost

Parameter	Dimension	Relation	Value
Input beam power	mW	P_0	1.500E+01
Diameter of image grating	mm	d_0	1.500E+00
Wavelength	mm	λ	4.000E-04
Fresnel zone plate diameter	mm	d_f	2.000E-01
Innermost zone radius of Fresnel zone plate	mm	ρ	1.000E-02
Fresnel zone plate focal length	mm	$f = \rho^2/\lambda$	2.500E-01
Free space propagation distance	mm	z	5.000E+00
The first order diffraction efficiency		η	4.053E-01
Diameter of diffraction zone plate	mm	$d_c = z^*d_f / f$	4.000E+00
Incident angle of a beam	rad	θ	2.014E-01
Numerical aperture of Fresnel zone plate		$N.A.= d_f/(2f)$	4.000E-01
Gamma		$\gamma = \sin\theta / N.A.$	5.000E-01
Radius of innermost of the first order moire zone plate	mm	$\rho_z = \lambda z/\rho$	2.000E-01
Area ratio of interference region to diffraction zone plate		r_1	3.910E-01
Area ratio of the innermost zone to interference region		r_2	1.000E-02
Power transmitted through Fresnel zone plate	mW	$P_t = P_0*(d_f/d_0)^2$	2.667E-01
Power of diffraction zone plate	mW	$P_c = 2\,\eta\, P_t$	2.162E-01
Power of the innermost zone	mW	$P_z = 2\, r_1\, r_2\, P_c$	1.690E-03

Figure A-3: An example of optical power calculation of the innermost zone of the first order moiré zone plate.

zone power of the moiré zone plate. The laser beam is assumed to have 15 mW, and the Fresnel zone plate has 0.4 in numerical aperture. About 0.01% of the input beam power is found to be used in the image grating metrology. Indeed, it poses a critical aspect of the image grating metrology using a Fresnel zone plate. As the small image grating period is approached, the input waves will be diffracted significantly, which reduces the optical power that can be measured at the sensor.

Appendix B

MATLAB scripts for Fresnel diffraction

B.1 prop.m

The program calculates two-dimensional diffraction pattern using the Fresnel diffraction approximation. The output is the amplitude distribution at the plane which is apart from the input plane by the distance z.

```
function f_out = prop(f_in,sizeo,sizei,lambda,z)
% Computes 2-D propatation using Fresnel diffraction approximation
%
% f_out: output field amplitude
%
% f_in: input field amplitude
% sizeo: size of scaled output plane
% sizei: size of input plane
% lambda: wavelength of light
% z: propagation distance                                          10

% check input parameters
if nargin<5 | nargin>6,
  disp('prop calling sequence:')
```

```
  disp('f_out = prop(f_in,sizeo,sizei,lambda,z)')
  disp(sprintf('\a'))
  return
end

% size of input plane
[m,n]=size(f_in);

m=fix(n/2);
if 2*m==n,
  M = [-m:m-1];
else
  M = [-m:m];
end
isgn = (-1).^M;
M = M.^2;

del = sizei / n;
lz = lambda * z;

% Compute convolution form of Fresnel diffraction integral

% (del)^2/(λz)
c1 = del^2 / lz;

% exp(jπξ^2λz);
dd = isgn.*exp(j*(π*c1)*M);

% Compute convolution kernel of Fresnel diffraction integral
% krnl = exp(jkz)/(jλz) * exp(jπ(ξ^2+η^2)/(λz))
% For simplicity, constant phase term neglected
krnl = -j/lz * (dd.'*dd);

% Compute Fourier transform
f_out = krnl.*f_in;
f_out = fft2(f_out);
```

```
% Compute the preceding term of the Fourier transform evaluated previously
% exp(jπλz*(x/λz)^2)
dd = isgn.*exp(j* pi * lz * M / (sizei^2));

f_out = (dd.'*dd) .*f_out;
```

B.2 propscale.m

The program calculates the appropriate size of the output plane based on the wavelength, the input plane size, and free propagation distance.

```
function so = propscale(f_in, sizein, lambda, z)
% The program calculates the proper output plane size.
%
% so: size of ouput
%
% f_in: input field
% sizein: size of input
% lambda: wavelength
% z: free progation distance

if nargin~=4
  disp('propscale calling sequence:')
  disp('so = propscale(f_in, sizein, lambda, z)')
  disp(sprintf('\a'))
  return
end

m=size(n);
if m(1)==1, m=n; else m=m(1); end

sizeout = m * lambda * abs(z) / sizein;
```

Appendix C

MATLAB scripts for moiré zone plate simulations

C.1 ZpIgDiffr.m

The program calculates the irradiance distribution of the observation plane, which is apart from the input plane by the propagation distance, z. The input waves are assumed to be unit-amplitude plane waves and the diffraction is evaluated based on the codes in [B].

```
clear all;
clc;

lambda = 0.3512;      % wavelength, in um
k = 2*pi/lambda;      % wave number

% range of input plane, in um
range = 100;
npts = 2048;

% generate the space of input plane
x = linspace(-range, range, npts);
y = linspace(-range, range, npts);
```

```
% free propagation distance, in um
z=100e3;

N = 14;                 % number of zones
rho = 8;                % the first zone radius, in um

% 2-D amplitude Fresnel zone plate
zp = zp2d(lambda, x, y, rho, N);

p = 1.44085;            % image grating period, in um
theta = asin(lambda/2/p);   % angle of incidence, in rad

% generate image grating
for m=1:npts
    for n=1:npts
        gratings(n,m) = exp(j*2*pi*sin(theta)/lambda * x(m)+j*pi)...
            +exp(-j*2*pi*sin(theta)/lambda * x(m));
    end;
end;

% superposition between image grating and Fresnel zone plate
f = zp.*gratings;

% free propagation using Fresnel diffraction approximation
sizei = 2*range;
sizeo = propscale(f,sizei,lambda,z);
g = prop(f, sizeo, sizei, lambda, z);

% calculate irradiance distribution in the observation plane
I = g.*conj(g);

% sample the innermost zone of the first-order moiré zone plate
rSamp = 1;
mask = circ2d(rSamp, x, y);
I = I.*mask;
```

```
% plot irradiance distribution. The observation plane is rescaled to
% millimeters.
scale = sizeo/sizei;
image(x(850:1200)*scale/1000, y(850:1200)*scale/1000, I(850:1200, 850:1200)*1.0e7);
xlabel('x (mm)');ylabel('y (mm)');
colormap(copper);
brighten(0.6);
```

C.2 Zp2d.m

The program generates two-dimensional amplitude Fresnel zone plate based on the discussion in 2.1.

```
function zp = zp2d(lambda, x, y, rho, N)
% zp2d.m
% It generates a Fresnel zone plate defined by the parameters described below.
% lambda: wavelength of light, in um
% x: x coordinates on input plane
% y: y coordinates on input plane
% rho: radius of the innermost zone
% N: number of zones

k = 2*pi/lambda;      % wave number
R = sqrt(N * rho^2);      % radius of Fresnel zone plate

% amplitude trasmittance function for Fresnel zone plate, Goodman, p.124
% Here, I only use fundamental frequency for simplicity. Namely, I don't use "sign" function.
% For reference,
% for m=1:npts
%       for n=1:npts
%             zoneplate(n,m) = (1/2) * (1 + sign(cos(pi/(rho^2) * (x(m)^2+y(n)^2))));
%       end;
```

```
% end;
for m=1:length(x)
    for n=1:length(y)
        zones(n,m) = (1/2) * (1 + (cos(pi/(rho^2) * (x(m)^2+y(n)^2))));
    end;
end;

% aperture of Fresnel zone plate
aperture = circ2d(R, x, y);

zp = zones.*aperture;
```

C.3 circ2d.m

The program generates a circle that is defined by the input radius.

```
function c = circ2d (Radius, x, y)
% This function generates a 2-D circle defined by Radius.
% Radius: radius of circle
% x: x coordinates
% y: y coordinates

% grid generation
[tempx, tempy] = meshgrid(x, y);

% circle generation, if d<radius, c=1;
d = sqrt(tempx.^2+tempy.^2);
c = (d <= Radius);
```

Appendix D

MATLAB scripts for image grating period calculations

D.1 PVdetector.m

The program obtains the locations (xPk, xVy) and values (Pk, Vy) of peaks and valleys in the input signal, based on the algorithm discussed in 3.1.1. It assumes that the signal begins and ends close to the centerline of the amplitude, i.e., the DC level.

```
function [xPk, Pk, xVy, Vy] = PVdetector(sig, thresPk, thresVy)
% It obtains the locations and values of peaks and valleys in the signal.
% If the signal begins below the threshold value,
% exceed the threshold at some location, and then return to a value below,
% one peak exists in that region. The valleys are also found in the same
% way.
%
% sig: signal
% thresPk: threshold value for peak detection
% thresVy: threshold value for valley detection                    10

% initialize output variables
xPk = [];
xVy = [];
```

```
Pk = [];
Vy = [];

% initialize temporary variables
xTemp = [];
yTemp = [];

% for peak, fpeak = 1, and for valley, fpeak = 0
fpeak = 0;

% search for peaks and valleys
for i=1:length(sig)
    % signal is above thresPK
    if sig(i) > thresPk
        fpeak = 1;
        xTemp = [xTemp, i];
        yTemp = [yTemp, sig(i)];
    % signal is below thresVy
    elseif sig(i) < thresVy
        fpeak = 0;
        xTemp = [xTemp, i];
        yTemp = [yTemp, sig(i)];
    % signal is between thresVy and thresPk
    else
        % if xTemp is filled
        if length(xTemp) ~= 0

            % fit the data stored in xTemp and yTemp to a second order
            % polynomial
            p = polyfit(xTemp, yTemp, 2);

            % Take the polynomial,
            q = polyder(p);

            % and obtain the root to find the location of peak or valley.
            r = roots(q);
```

```
            % calculate the value of peak or valley using the root found
            % before
            y = polyval(p, r);

            % if it is peak, append it to the array of peaks.
            if fpeak == 1
                x_pk = [x_pk, r];
                pk = [pk, y];
            % if it is valley, append it to the array of valleys.
            elseif fpeak == 0
                x_vy = [x_vy, r];
                vy = [vy, y];
            end;
            x_temp = [];
            y_temp = [];
        end;
    end;
end;
```

D.2 countCycles.m

The program calculates total number of cycles, $N = N_i + N_m + N_f$. The returned value is used to obtain image grating period by $\Lambda = D/N$.

```
function cnt = countCycles(yi, yf, xPk, Pk, xVy, Vy)
% countCycles returns total number of cycles in the signal, N = Ni + Nm +
% Nf.

% yi: initial readout before stage moves
% yf: final readout after stage stops
% xPk: peak locations
```

```
% Pk: peak values
% xVy: valley locations
% Vy: valley values

% calculate number of peaks and valleys
numPk = length(xPk);
numVy = length(xVy);

% temporary values
totPk = 0;
totVy = 0;

% calculate average peak value
for i=1:numPk-1
    totPk = totPk+Pk(i);
end;
avePk = totPk/numPk;

% calculate average valley value
for i=1:numVy-1
    totVy = totVy+Vy(i);
end;
aveVy = totVy/numVy;

% calculate A and B of a sinusoidal
A = abs(avePk-aveVy)/2;
B = abs(avePk+aveVy)/2;

% calculate fractional cycles, Ni and Nf
Ni = 1/4 - 1/(2*pi)*abs(asin(abs(yi-B)/A));
Nf = 1/4 - 1/(2*pi)*abs(asin(abs(yf-B)/A));

% calculate completed cycles, Nm
if numPk > numVy
    Nm = numVy;
elseif numPk == numVy
```

```
    Nm = numPk−0.5;
else
    Nm = numPk;
end;

cnt = Ni+Nm+Nf;
```

Appendix E

MATLAB scripts for optical power contrast fluctuations

E.1 contCalc.m

The program performs optical power contrast calculations with varying image grating period. For simplicity, the code is written for one-dimensional case. It produces two plots: optical power variation vs. image grating period and contrast variation vs. image grating period.

```
clear all;
clc;

lambda = 0.3512;      % wavelength, in um
k = 2*pi/lambda;      % wave number

% range of input plane, in um
range = 100;
npts = 2048;

% generate grids
x = linspace(-range, range, npts);
dx = 2*range/npts;
```

```
z=100e3;          % free propagation distance, in um
sampA = 1;        % sample area for power calculation, in mm

N = 14;           % number of zones
rho = 8;          % the innermost zone radius, in um

% generate 1-D amplitude Fresnel zone plate
zp = zp1d(lambda, x, rho, N);

% initialize all arrays and parameters
arrN = [];        % numerator, N(Λ)
arrD = [];        % denominator, D(Λ)
arrC = [];        % contrast, C(Λ)
i = 0;            % enumerator
step = 0.05;      % step size for relative motion of image grating and Fresnel zone plate

% p: image grating period.
% p is represented by Λ in the thesis.
for p = 1.2:0.01:1.8

    % incident angle
    theta = asin(lambda/2/p);

    i = i+1;

    d = 0;
    maxPwr = 0;
    minPwr = 0;
    arrPwr = [];

    for index=0:55

        % clear arrays
        clear gratings;
```

```
    % displacement of image grating relative to Fresnel zone plate
    d = index*step;

    % generate grating
    gratings = exp(j*2*pi*sin(theta)/lambda * (x+d))+exp(-j*2*pi*sin(theta)/lambda * (x+d));

    % superposition between image grating and Fresnel zone plate
    f = zp.*gratings;

    % free propagation through z
    sizei = 2*range;
    sizeo = length(f) * lambda * abs(z) / sizei;
    scale = sizeo/sizei;
    g = prop1d(f, sizeo, sizei, lambda, z);

    % evaluate intensity
    I = g.*conj(g);

    % sample innermost zone of the first-order moiré zone plate.
    mask = circ(sampA, x);
    I = I.*mask;

    % evaluate optical power
   arr_pwr(index+1) = sum(I*dx*scale);
end;

% obtain max. and min. power
maxPwr = max(arrPwr);
minPwr = min(arrPwr);

% image grating period array
arrp(i) = p;

% D(Λ): average power
arrD(i) = (maxPwr + minPwr)/2;
```

```
    % N(Λ) assuming the initial phase difference of two beams is zero.
    arrN(i) = arrPwr(1) - arrD(i);

    % contrast array
    arrC(i) = (maxPwr - minPwr) / (maxPwr + minPwr);
end;

% plot N(Λ), D(Λ), and P(Λ)
figure;
plot(arrp, arrN, 'r');
hold on;
plot(arrp, arrD, 'b');
hold on;
plot(arrp, arrN+arrD, ':k');
hold on;
legend('N(Λ)','D(Λ)','P(Λ)');
xlabel('Λ');
ylabel('Power (a.u.)');
xlim([1.208 1.785]);

% plot contrast vs. image grating period, C(\Lambda)
figure;
plot(arrp, arrC, 'k');
xlim([1.208 1.785]);
xlabel('Λ');
ylabel('Contrast');
```

Bibliography

[1] M. L. Schattenburg, C. Chen, P. N. Everett, J. Ferrera, P. Konkola, and H. I. Smith. Sub-100 nm metrology using interferometrically produced fiducials. *J. Vac. Sci. and Technol.*, **B** 17, 2692, 1999.

[2] Juan Ferrera Nanometer-Scale Placement in Electron-Beam Lithography. PhD dissertation, Massachusetss Institute of Technology, Department of Electrical Engineering and Computer Science, June 2000.

[3] Juan Ferrera, M. L. Schattenburg, and Henry I. Smith. Analysis of distortion in interferometric lithography. *J. Vac. Sci. and Technol.*, **B** 14, 4009, 1996.

[4] Carl G. Chen, Paul T. Konkola, R. K. Heilmann, G. S. Pati, and M. L. Schattenburg. Image metrology and system controls for scanning-beam interference lithography. *J. Vac. Sci. and Technol.*, **B** 19, 2335, 2001.

[5] Paul T. Konkola, Carl G. Chen, Ralf K. Heilmann, and Mark L. Schattenburg. Beam steering system and spatial filtering applied to interference lithography. *J. Vac. Sci. and Technol.*, **B** 18, 3282, 2000.

[6] Ralf K. Heilmann, Paul T. Konkola, Carl G. Chen, and Mark L. Schattenburg. Relativistic correction in displacement measuring interferometry. *J. Vac. Sci. and Technol.*, **B** 18, 3277, 2000.

[7] Ralf K. Heilmann, Paul T. Konkola, Carl G. Chen, and Mark L. Schattenburg. Digital heterodyne interference fringe control system. *J. Vac. Sci. and Technol.*, **B** 19, 2342, 2001.

[8] W.A. Podgorski, D.A. Content, J.H. Hair, R. Petre, T.T. Saha, M.L. Schattenburg, J. Stewart and W.W. Zhang. Constellation-X Spectroscopy X-ray Telescope assembly and alignment. *Proc. SPIE 4851, X-ray and Gamma-ray Telescopes and Instruments for Astronomy.*, SPIE, Bellingham, WA, 2002.

[9] R. Petre, W.W. Zhang, D.A. Content, T. T. Saha, J. Stewart, J.H. Hair, D.Nguyen, W.A. Podgorski, W.R. Davis, Jr., M.D. Freeman, L.M. Cohen, M.L. Schattenburg, R.K. Heilmann, Y. Sun and C. Forest. Constellation-X Spectroscopy X-ray Telescope (SXT). *Proc. SPIE 4851, X-ray and Gamma-ray Telescopes and Instruments for Astronomy.*, SPIE, Bellingham, WA, 2002.

[10] G. S. Pati, R. K. Heilmann, P. T. Konkola, C. Joo, C. G. Chen, E. Murphy, and M. L. Schattenburg. Generalized scanning beam interference lithography system for patterning gratings with variable period progressions. *J. Vac. Sci. and Technol.*, **B** 20, 2617, 2002.

[11] William N. Partlo, Charles H. Fields, and William G. Oldham. Direct aerial image measurement as a method of testing high numerial aperture microlithographic lenses. *J. Vac. Sci. and Technol.*, **B** 11, 2686, 1993.

[12] David Attwood. *Soft X-rays and extreme ultraviolet radiation: principles and applications.* Cambridge, Cambridge Unversity Press, 2000.

[13] Lord Rayleigh. Wave Theory. *Encylopaedia Brittanica*, Ninth Ed., Vol 24, 1998.

[14] Gilbert Strang *Calculus.* Wellesley, Mass., Wellesley-Cambridge Press, 1991.

[15] Joseph W. Goodman *Introduction to Fourier Optics.* Second ed., McGraw-Hill, Boston, MA, 1996.

[16] G. Harburn, T. R. Welberry, and R. P. Williams. in Selected Papers on Zone Plates. *Selected Papers on Zone Plates*, edited by J. Ojeda-Castaneda and C. Gomez-Reino, SPIE, Bellingham, WA, 1996.

[17] Chulmin Joo, G. S. Pati, Carl G. Chen, Paul T. Konkola, Ralf K. Heilmann, Mark L. Schattenburg, Alexander Liddle, and Erik H. Anderson. Precision fringe metrology using a Fresnel zone plate. *J. Vac. Sci. and Technol.*, **B** 20, 3075, 2002.

[18] Christopher Palmer *Diffraction grating handbook.* Fifth ed., Spectra-Physics, Richardson Gratings, Rochester, NY, 2002.

[19] Carl G. Chen Beam alignment and image metrology for scanning beam interference lithography - Fabricating gratings with nanometer phase accuracy. PhD dissertation, Massachusetss Institute of Technology, Department of Electrical Engineering and Computer Science, June 2003.

[20] Frank C. Demarest. High resolution, high speed, low data age uncertainty, heterodyne displacement measuring electronics. *Meas. Sci. Technol.*, 9:1024-1030, 1998.

[21] Carl G. Chen, Paul T. Konkola, Ralf K. Heilmann, Chulmin Joo, and Mark L. Schattenburg. Nanometer-accurate grating fabrication with scanning beam interference lithography. *Proc. SPIE*, 4936:126-134, 2002.

[22] Paul T. Konkola Design and analysis of a scanning beam interference lithography system for patterning gratings with nanometer-level distortions. PhD dissertation, Massachusetss Institute of Technology, Department of Mechanical Engineering, June 2003.

[23] Erik H. Anderson, Deirdre L. Olynick, Bruce Harteneck, Eugene Veklerov, Gregory Denbeaux, Weilun Chao, Angelic Lucero, Lewis Johnson, and David Attwood. Nanofabrication and diffractive optics for high-resolution x-ray applications. *J. Vac. Sci. and Technol.*, **B** 20, 2970, 2000.

[24] ADE Technologies. Capacitance gauge, Model 4810.

[25] National Instruments Corporation. *NI 6034E/6035E/6036E User Manual*, May 2001. Part Number 322339B-01.

[26] Alan V. Oppenheim, Ronald W. Schafer, and John R. Buck. *Discrete-Time Signal Processing*. Prentice Hall, Second Ed., 1999.

[27] John G. Proakis and Dimitris G. Manolakis. *Digital Signal Processing: Principles, Algorithms, and Applications*. Prentice Hall, Third Ed., 1995.

[28] K. Oka, M. Tsukada, and Y. Ohtsuka. *Meas. Sci. Technol.*, **2** 106, 1991.

[29] N. M. Oldham, J. A. Kramar, P. S. Hetrick, and E. C. Teague. *Precis. Eng.*, **15** 173, 1993.

[30] Stanford Research Systems. *Model SR830 DSP Lock-In Amplifier*, June 1993.